The Astrophysical Journal, 819:66 (21pp), 2016 March 1 doi:10.3847/0004-637X/819/1/66

A MULTI-WAVELENGTH STUDY OF STAR FORMATION ACTIVITY IN THE S235 COMPLEX

L. K. Dewangan[1,2], D. K. Ojha[3], A. Luna[1], B. G. Anandarao[2], J. P. Ninan[3], K. K. Mallick[3], and Y. D. Mayya[1]
[1] Instituto Nacional de Astrofísica, Óptica y Electrónica, Luis Enrique Erro # 1, Tonantzintla, Puebla, C.P. 72840, México; lokeshd@prl.res.in
[2] Physical Research Laboratory, Navrangpura, Ahmedabad—380 009, India
[3] Department of Astronomy and Astrophysics, Tata Institute of Fundamental Research, Homi Bhabha Road, Mumbai 400 005, India
Received 2015 October 7; accepted 2016 January 17; published 2016 February 29

ABSTRACT

We have carried out an extensive multi-wavelength study to investigate the star formation process in the S235 complex. The S235 complex has a spherelike shell appearance at wavelengths longer than 2 μm and harbors an O9.5V type star approximately at its center. A near-infrared extinction map of the complex traces eight subregions (having $A_V > 8$ mag), and five of them appear to be distributed in an almost regularly spaced manner along the spherelike shell surrounding the ionized emission. This picture is also supported by the integrated ^{12}CO and ^{13}CO intensity maps and by Bolocam 1.1 mm continuum emission. The position–velocity analysis of CO reveals an almost semi-ringlike structure, suggesting an expanding H II region. We find that the Bolocam clump masses increase as we move away from the location of the ionizing star. This correlation is seen only for those clumps that are distributed near the edges of the shell. Photometric analysis reveals 435 young stellar objects (YSOs), 59% of which are found in clusters. Six subregions (including five located near the edges of the shell) are very well correlated with the dust clumps, CO gas, and YSOs. The average values of Mach numbers derived using NH_3 data for three (East 1, East 2, and Central E) out of these six subregions are 2.9, 2.3, and 2.9, indicating these subregions are supersonic. The molecular outflows are detected in these three subregions, further confirming the ongoing star formation activity. Together, all these results are interpreted as observational evidence of positive feedback of a massive star.

Key words: dust, extinction – H II regions – ISM: clouds – ISM: individual objects (S235) – stars: formation – stars: pre-main sequence

1. INTRODUCTION

The energetics of massive stars can strongly influence the surroundings (Zinnecker & Yorke 2007). Massive stars can destroy star-forming clouds (i.e., negative feedback) and can also trigger star formation (i.e., positive feedback), leading to the formation of a new generation of stars including young massive star(s) (Deharveng et al. 2010). However, the feedback processes of massive stars are still poorly understood.

The extended star-forming region S235 is known to be a part of the giant molecular cloud G174+2.5 in the Perseus Spiral Arm (e.g., Heyer et al. 1996) and contains two known sites: the S235 complex and the S235AB region (see Figure 1 in Dewangan & Anandarao 2011 and also Figure 1 in Kirsanova et al. 2014). The present work is focused on the S235 complex and does not include the S235AB region. Different values of the distance (1.36, 1.59, 1.8, 2.1, and 2.5 kpc) to the extended star-forming region S235 have been reported in the literature (e.g., Georgelin et al. 1973; Israel & Felli 1978; Evans & Blair 1981; Brand & Blitz 1993; Burns et al. 2015; Foster & Brunt 2015). In the present work, we have chosen a distance of 1.8 kpc following Evans & Blair (1981), which is an intermediate value of the published distance range. The H II region associated with the S235 complex is predominantly ionized by a single massive star, BD+35°1201, of O9.5V type (Georgelin et al. 1973). The S235 complex has been studied using multiple data sets spanning near-infrared (NIR) to radio wavelengths. The S235 complex is known as an active site of star formation, harboring young stellar clusters (e.g., Kirsanova et al. 2008; Camargo et al. 2011; Dewangan & Anandarao 2011; Chavarría et al. 2014) associated with known star-forming subregions, namely East 1, East 2, and the Central region (e.g., Kirsanova et al. 2008). In our previous work on the S235 complex using *Spitzer*-IRAC data (Dewangan & Anandarao 2011, hereafter Paper I) we detected several young stellar objects (YSOs) including a high mass protostellar object (HMPO) candidate as well as signatures of outflow activities. Using ^{13}CO (1−0) line data, Kirsanova et al. (2008) found three molecular gas components (i.e., $-18\,\mathrm{km\,s^{-1}} < V_{\rm lsr} < -15\,\mathrm{km\,s^{-1}}$ (red), $-21\,\mathrm{km\,s^{-1}} < V_{\rm lsr} < -18\,\mathrm{km\,s^{-1}}$ (central), and $-25\,\mathrm{km\,s^{-1}} < V_{\rm lsr} < -21\,\mathrm{km\,s^{-1}}$ (blue)) in the direction of the S235 complex. However, the complex is well traced in mainly two molecular gas components (central and blue). More recently, Kirsanova et al. (2014) derived physical parameters of dense gas (i.e., gas density and temperature) in subregions of the complex using ammonia (NH_3) line observations. However, the properties of dense gas have not been explored with respect to the ionizing star location. Previous studies indicated that the S235 H II region is interacting with its surrounding molecular cloud and the S235 complex has been cited as a possible site of triggered star formation (Kirsanova et al. 2008, 2014; Camargo et al. 2011).

Spitzer images revealed that the complex has a spherelike shell morphology and the ionizing star is approximately located at its center (see Figure 1 given in Paper I). In addition to the observed interesting morphology, the complex is a relatively nearby star-forming site, making it a promising site to study the feedback of a massive star. In spite of the numerous existing observations and interpretations, the feedback of an O9.5V type star is not systematically explored in the S235 complex. The aim of the present work is to study the physical processes governing the interaction and feedback effect of a massive star on its surroundings.

In order to address the above aim, we revisited the S235 complex using high sensitivity United Kingdom Infra-Red Telescope (UKIRT) Infrared Deep Sky Survey (UKIDSS) NIR

data, the Giant Metre-wave Radio Telescope (GMRT) 610 MHz radio continuum map, and dust continuum 1.1 mm data in conjunction with the published narrow-band H_2 map, *Spitzer* mid-infrared (MIR) data, NH_3 line data, the NRAO VLA Sky Survey (NVSS) 1.4 GHz continuum map, and CO line data. We performed a detailed study of the distribution and kinematics of molecular gas in the complex. In order to systematically explore the feedback of a massive star, we estimated various pressure components (such as pressure of an H II region, radiation pressure, stellar wind pressure, pressure exerted by the self-gravitating molecular cloud, and the ratio of thermal to non-thermal gas pressure). For a detailed study of the embedded young population in the complex, we employed different color–color and color–magnitude diagrams obtained using NIR and MIR data, as well as extinction maps generated from NIR data and surface density analysis. Additionally, the physical properties of gas derived using the line and continuum data were investigated.

In Section 2, we provide the description of various data sets along with reduction procedures. In Section 3, we summarize the results related to the physical environment and pointlike sources. The possible star formation scenario is discussed in Section 4. Our main conclusions are summarized in Section 5.

2. DATA AND ANALYSIS

Multi-wavelength data are employed to study the physical conditions in the S235 complex. The size of the selected region is $\sim 17\farcm6 \times 15\farcm5$, centered at $\alpha_{2000} = 05^h40^m57^s.8$, $\delta_{2000} = +35^\circ.51'13''$, corresponding to a physical scale of about 9.2 pc × 8.1 pc at a distance of 1.8 kpc.

2.1. Narrow-band H_2 image

Narrow-band H_2 ($\nu = 1-0$ S(1) at $\lambda = 2.122\ \mu$m ($\Delta\lambda = 0.032\ \mu$m)) imaging data of the S235 complex were obtained from the survey of extended H_2 emission (Navarete et al. 2015) conducted at the Canada–France–Hawaii Telescope (CFHT), Mauna Kea, HI, using the Wide-field InfraRed Camera (WIRCam). The observations were performed with an average seeing of $\sim 0\farcs7$. The survey also provided *K*-band continuum ($\lambda = 2.218\ \mu$m; $\Delta\lambda = 0.033\ \mu$m) images, which were used to get the final continuum-subtracted H_2 map. Note that the H_2 image published by Navarete et al. (2015) contains only the East 2 and Central star-forming subregions (see source IDs 164 and 165 in Table B2 given in Navarete et al. 2015), while the H_2 image in this work is presented for a larger area $\sim 10\farcm7 \times 9\farcm9$ toward the complex. One can find more details about the survey in the work of Navarete et al. (2015).

2.2. Near-infrared Data

We obtained deep NIR photometric *JHK* images and the magnitudes of point sources in the region ($\sim 17\farcm6 \times 15\farcm5$) from the UKIDSS sixth archival data release (UKIDSSDR6plus) of the Galactic Plane Survey (GPS; Lawrence et al. 2007). The survey uses the UKIRT Wide Field Camera (WFCAM; Casali et al. 2007). Following the selection conditions given in Lucas et al. (2008), we retrieved only reliable NIR sources in the region. One can also find more details about the selection procedure of the GPS photometry in the work of Dewangan et al. (2015). Two Micron All Sky Survey (2MASS; Skrutskie et al. 2006) data were obtained for bright sources that were saturated in the GPS catalog. We found 2444 sources detected in all three NIR (*JHK*) bands. Additionally, 326 sources were selected which had detections only in the *H* and *K* bands.

2.3. Spitzer Data

The photometric images (3.6–24 μm) of the S235 complex were obtained from the *Spitzer Space Telescope* Infrared Array Camera (IRAC; Fazio et al. 2004) and the Multiband Imaging Photometer (MIPS; Rieke et al. 2004). The final processed IRAC images (3.6–8.0 μm) and photometry of point sources were taken from Paper I. MIPS 24 μm observations were retrieved from the *Spitzer* public archive[4] and were carried out in MIPS scan mode on 2008 April 15 (Program id 40005; PI: Giovanni Fazio). The MIPS mosaic at 24 μm was generated using the basic calibrated data (BCD) images.

2.4. Dust Continuum 1.1 mm Data

The Bolocam 1.1 mm image (Aguirre et al. 2011) and Bolocam source catalog at 1.1 mm (v2.1; Ginsburg et al. 2013) were obtained from the Bolocam Galactic Plane Survey (BGPS). The effective FWHM of the 1.1 mm map is $\sim 33''$.

2.5. Radio Continuum Data

We used the archival radio continuum data at 610 MHz (50 cm) and 1.4 GHz (21 cm). The 1.4 GHz map was retrieved from the NVSS archive. The beam size of the NVSS image is $\sim 45''$ (Condon et al. 1998). The 610 MHz continuum data were observed on 2005 June 18–19 (Project Code: 08SKG01) and were retrieved from the GMRT archive. GMRT radio data reduction was carried out using AIPS software in a manner similar to that described in Mallick et al. (2013). Since the S235 complex was away from the center of the observed field, the primary beam correction for 610 MHz was also carried out using the AIPS PBCOR task and parameters from the GMRT manual.[5] The synthesized beam size of the final 610 MHz map is $\sim 48'' \times 44\farcs2$.

2.6. Molecular CO Line Data

The $J = 1-0$ lines of ^{12}CO and ^{13}CO data were observed from the Five College Radio Astronomy Observatory (FCRAO) 14 m telescope in New Salem, MA. The FCRAO beam sizes were $45''$ and $46''$ for ^{12}CO and ^{13}CO, respectively. The S235 complex was observed as part of the Extended Outer Galaxy Survey (E-OGS, Brunt 2004), which extends the coverage of the FCRAO Outer Galaxy Survey (OGS, Heyer et al. 1998) to Galactic longitude $l = 193^\circ$, over a latitude range of $-3^\circ.5 \leqslant b \leqslant +5^\circ.5$. However, the data cubes of S235 complex were further re-processed and a document describing the re-processing data methods is given in Brunt (2004; see also C. M. Brunt et al. 2016, in preparation). These CO data cubes were obtained from M. Heyer and C. Brunt (2015, private communication).

2.7. Other Data

We utilized the publicly available archival *WISE*[6] (Wright et al. 2010) image at 12 μm (spatial resolution $\sim 6''$). We also

[4] See http://sha.ipac.caltech.edu/applications/Spitzer/SHA/

[5] http://gmrt.ncra.tifr.res.in/gmrt_hpage/Users/doc/obs_manual.pdf

[6] *Wide-field Infrared Survey Explorer*, which is a joint project of the University of California and the JPL, Caltech, funded by NASA.

used previously published NH_3 line data from Kirsanova et al. (2014).

3. RESULTS

3.1. Mid-infrared and Radio Continuum Images

The most prominent feature of the S235 complex observable in the infrared regime, the spherelike shell morphology, is detected at wavelengths longer than 2 μm (see Figure 1). Figure 1(a) is a three-color composite image made using MIPS 24 μm in red, *WISE* 12.0 μm in green, and IRAC 8.0 μm in blue. Figure 1(b) shows a three-color composite image using MIPS 24 μm (red), IRAC 4.5 μm (green), and UKIDSS 2.2 μm (blue). Radio continuum contours at 1.4 GHz and 610 MHz are also overlaid on the color-composite images in Figures 1(a) and (b), respectively. These radio continuum contours trace the ionized emission in the S235 complex. The distribution of ionized emission is almost spherical in both radio maps. The location of a previously characterized O9.5V star (BD +35°1201) appears at the peak of radio continuum emission. The bulk of the ionized emission, as traced at the sensitivity levels shown in Figures 1(a) and (b), is well located inside the spherelike shell, as highlighted by a circle in Figure 1(a). The radio emission at 610 MHz appears elongated in the north direction as highlighted by an arrow (see Figure 1(b)). This particular feature does not appear to be seen in the NVSS 1.4 GHz map. The *WISE* 12 μm band is dominated by the 11.3 μm polycyclic aromatic hydrocarbon (PAH) emission as well as the warm dust continuum emission. The 24 μm image shows the warm dust emission, whereas the 8 μm band contains PAH emission features at 7.7 and 8.6 μm (including the continuum). In Figure 1, we notice that the warm dust emission is surrounded by 8 μm emission. Furthermore, the correlation of the warm dust and ionized emission is evident, which has generally been found in H II regions (e.g., Deharveng et al. 2010; Paladini et al. 2012). In addition to the extended emission, the embedded stellar contents are visually seen around the spherelike shell. The different subregions (East 1, East 2, North, Northwest, Central W, Central E, Southwest, and South) in the S235 complex are shown in Figure 1(b). Note that three subregions (East 1, Southwest, and South) are located away from the edges of the spherelike shell (see Figure 1). There is noticeable nebular emission seen between the East 1 subregion and the spherelike shell, which is designated as the eastern emission wall in Figure 1(a). The Central E subregion contains two bright sources, namely EB IRS 1/G173.6328+02.8064 (hereafter, IRS 1) and EB IRS 2/G173.6339+02.8218 (hereafter, IRS 2) (Evans & Blair 1981) with previously estimated luminosities of $\sim 2.5 \times 10^3\, L_\odot$ and $\sim 1.5 \times 10^3\, L_\odot$ (Evans et al. 1981), respectively. Furthermore, radio continuum emissions are absent toward these two sources (IRS 1 and IRS 2), as pointed out by Nordh et al. (1984). Combining this information with the radio continuum data presented in this work, one can note that no radio continuum emission peaks are seen toward the subregions. Figure 1(b) shows the enhanced 4.5 μm and *K*-band extended emission features in the East 1 and East 2 subregions. In Paper I, the signatures of outflow activities were found toward East 1 and East 2 subregions due to the presence of shock-excited H_2 emissions as revealed by the IRAC ratio maps. Note that the embedded sources in the East 1 subregion appear to be separated from the spherelike shell by the eastern emission wall (see Figure 1(a)).

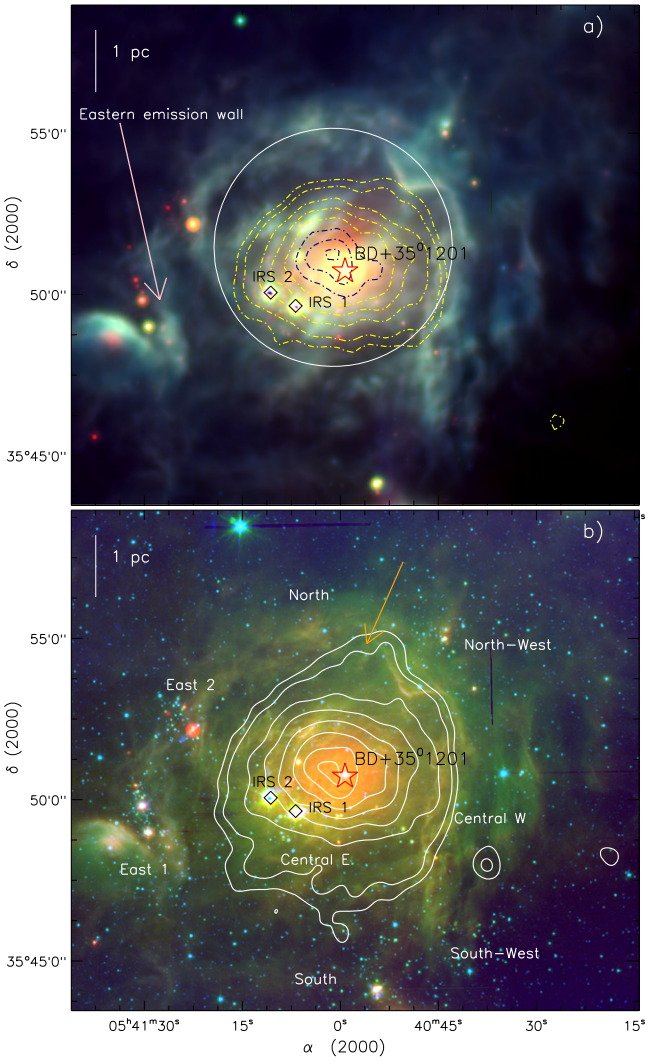

Figure 1. MIR and NIR emissions toward the S235 complex (the size of the selected field $\sim 17\farcm6 \times 15\farcm5$ (or 9.2 pc × 8.1 pc); centered at $\alpha_{2000} = 05^h40^m57\fs8$, $\delta_{2000} = +35°51'13''$). (a) The image is the result of the combination of three bands: 24 μm in red (MIPS), 12.0 μm in green (*WISE*), and 8.0 μm in blue (IRAC). Contours of NVSS 1.4 GHz radio continuum emission (beam size ~45″) are superimposed with 5%, 10%, 25%, 40%, 55%, 70%, 85%, and 98% of the peak value (i.e., 0.124 Jy/beam). The big circle highlights a spherelike shell morphology seen in *Spitzer* images. A nebular emission is designated as the eastern emission wall (see Section 3.1 for more details). (b) Color-composite map using *Spitzer* MIPS 24 μm (red), IRAC 4.5 μm (green), and UKIDSS K (blue) images. GMRT 610 MHz radio continuum contours (beam size $\sim 48'' \times 44\farcs2$) are in white with levels of 5%, 10%, 25%, 40%, 55%, 70%, 85%, and 98% of the peak value (i.e., 0.158 Jy/beam). Different subregions are also labeled in the map (see the text for more details). In both the panels, the positions of two bright sources (IRS 1 and IRS 2) and an O9.5V star (BD+35°1201) are marked with diamond and star symbols, respectively. The scale bar on the top left shows a size of 1 pc at a distance of 1.8 kpc in both the figures.

3.2. Near-infrared Extinction Map

The visual extinction (A_V) map of the S235 complex is generated using the publicly available GPS NIR (JHK)

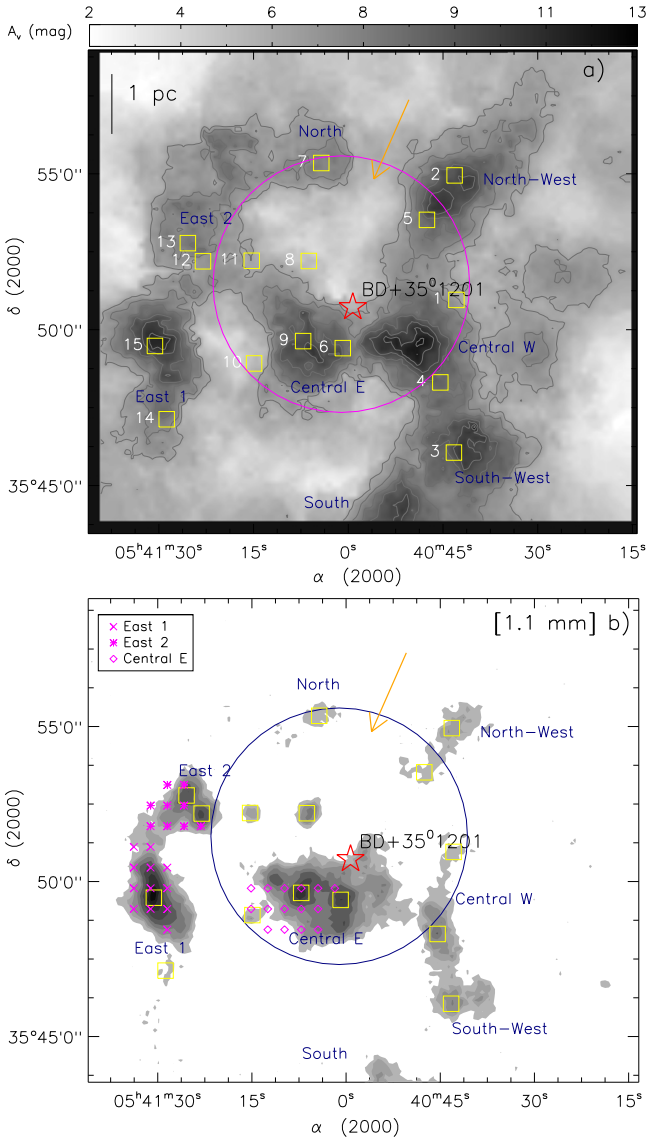

Figure 2. (a) Visual extinction map of the S235 complex obtained using the NIR data. (b) Contour map of Bolocam 1.1 mm dust continuum emission (beam size ∼33″). The contour levels are 8%, 15%, 20%, 30%, 40%, 55%, 70%, 85%, and 95% of the peak value, i.e., 1.2 Jy/beam. The positions of previously observed NH_3 line observations in the East 1 (x), East 2 (*), and Central E (◊) subregions are marked (see the text for details and also Table 2). The positions of dust clumps at 1.1 mm are marked by yellow square symbols in both the panels and are labeled in panel "a" (see Table 1). In both the panels, other marked symbols and labels are similar to those shown in Figure 1.

photometric data. The extinction value of individual stars was computed using a color excess along the line of sight ($E(H-K) = (H-K)_{\rm obs} - \langle (H-K)_0 \rangle$; see the equation given in Lada et al. 1994) using the reddening laws of Indebetouw et al. (2005). The $\langle (H-K)_0 \rangle$ is the mean intrinsic color of the stars, which was determined to be ∼0.25 from the nearby control field (similar size as target region; central coordinates: $\alpha_{J2000} = 05^{\rm h}43^{\rm m}35\overset{\rm s}{.}8$, $\delta_{J2000} = +35°20'20\overset{''}{.}4$). The extinction map was created from the mean value of 40 nearest neighbors. The resultant A_V map of the S235 complex is shown in Figure 2(a), which allows one to trace several embedded subregions in the complex. All these subregions are indicated in Figure 2(a) and are highlighted in Figure 1(b) based on the visual appearance of stellar contents. The A_V values vary between 2 and 12.5 mag with an average of about 5.8 mag. The A_V map also resembles the spherelike morphology as highlighted in Figure 1(a), except in the north direction, where it seems to be broken (shown by an arrow in Figure 2(a)).

Fifteen Bolocam dust continuum clumps at 1.1 mm were retrieved from the Bolocam source catalog (v2.1) and are shown in Figure 2(a). Figure 2(a) illustrates a correlation between extinction and dust clumps. Most of the clumps are located in the region having A_V greater than 8 mag.

3.3. Clump Properties

Dust continuum emission is known to trace the dense and cold regions. In Figure 2(b), we show Bolocam dust continuum emission at 1.1 mm, which is seen toward all the marked subregions in Figure 1(b). It is important to note that previously published SCUBA/JCMT 850 μm data (beam size ∼14″) are not available toward the North and Northwest subregions of the S235 complex (e.g., Klein et al. 2005; Francesco et al. 2008). Therefore, the 1.1 mm data (beam size ∼33″) provide a more complete information of the dense and cold regions of the S235 complex. The 15 clumps identified in the 1.1 mm map are also presented in Figure 2(b). The association of clump(s) with each subregion is listed in Table 1. Five subregions (i.e., Northwest, Central W, Central E, East 1, and East 2) contain at least two clumps, while another two subregions (i.e., Southwest and North) are associated with a single clump. In order to derive the gas mass M_g for each clump at 1.1 mm emission, the following formula has been utilized (Hildebrand 1983):

$$M_g = \frac{D^2\, S_\nu\, R_t}{B_\nu(T_d)\, \kappa_\nu}, \quad (1)$$

where S_ν is the integrated 1.1 mm flux (Jy), D is the distance (kpc), R_t is the gas-to-dust mass ratio (assumed to be 100), B_ν is the Planck function for a dust temperature T_d, and κ_ν is the dust absorption coefficient. In the calculation, we use $\kappa_\nu = 1.14\,{\rm cm^2\,g^{-1}}$ (e.g., Enoch et al. 2008; Bally et al. 2010), $D = 1.8$ kpc, and $T_d = 20$ K (an average temperature value estimated from NH_3 line data; see Kirsanova et al. 2014 for more details). The masses computed from the observed dust continuum data are listed in Table 1. The total gas mass of the 15 clumps comes out to be ∼1179 $M_\odot$. The clump masses vary between 7 $M_\odot$ and 285 $M_\odot$. All but three of the clumps have masses below 100 $M_\odot$. These three clumps are associated with the Central E (clump IDs 6 and 9) and East 1 (clump ID 15) subregions and have masses more than 200 $M_\odot$ (see Table 1). In an earlier work on the S235 complex (excluding the North and Northwest subregions), Klein et al. (2005) selected 13 dust emission clumps in the JCMT SCUBA 850 μm survey (beam size ∼14″; see Figure 1 of IRAS 05377+3548 in Klein et al. 2005). They estimated a mass range of clumps between 10 and 120 $M_\odot$, using an average dust temperature of 20 K, a gas-to-dust mass ratio of 150, and a distance of 1.8 kpc. Kirsanova et al. (2014) also computed a mass range of dense gas in the clumps between 12 and 250 $M_\odot$ (see Table 6 in Kirsanova et al. 2014). Considering the clump masses estimated in the present work, one can find a noticeable difference in the clump mass at the high end of the estimated range compared to previous works. At the low end of the range,

Table 1
Bolocam Clumps at 1.1 mm (see Figure 2)

ID	BGPS Name	R.A. [2000]	decl. [2000]	D_s (pc)	$R_{\rm eff}$ ″(pc)	S_ν [Jy]	M_g ($M_\odot$)	$N(H_2)$ (10^{22} cm^{-2})	$P_{\rm clump}$ (10^{-10} dynes cm^{-2})	Subregion
1	G173.570+02.749	05:40:42.9	+35:50:57	1.75	50.53(0.44)	0.549	23.10	1.10	0.13	Central W
2†	G173.515+02.785	05:40:43.2	+35:54:57	2.80	80.20(0.70)	1.345	56.59	2.69	0.12	Northwest
3	G173.640+02.707	05:40:43.3	+35:46:04	2.98	57.77(0.50)	1.429	60.12	2.86	0.54	Southwest
4	G173.613+02.733	05:40:45.4	+35:48:18	1.94	59.10(0.52)	1.947	81.92	3.90	0.85	Central W
5†	G173.543+02.785	05:40:47.6	+35:53:31	1.92	⋯	0.193	8.12	0.39	⋯	Northwest
6†	G173.625+02.787	05:41:00.9	+35:49:24	0.71	95.09(0.83)	5.128	215.75	10.30	0.91	Central E
7†	G173.546+02.849	05:41:04.3	+35:55:21	2.48	37.49(0.33)	0.438	18.43	0.88	0.26	North
8	G173.594+02.827	05:41:06.2	+35:52:12	1.07	⋯	0.482	20.28	0.96	⋯	⋯
9†	G173.633+02.807	05:41:07.2	+35:49:38	1.01	93.12(0.81)	5.978	251.53	12.0	1.36	Central E
10†	G173.657+02.823	05:41:14.9	+35:48:55	1.91	⋯	0.255	10.73	0.51	⋯	Central E
11	G173.610+02.853	05:41:15.3	+35:52:13	1.87	⋯	0.216	9.10	0.43	⋯	⋯
12†	G173.625+02.875	05:41:23.0	+35:52:12	2.63	⋯	1.041	43.80	2.08	⋯	East 2
13†	G173.621+02.887	05:41:25.4	+35:52:47	2.97	44.71(0.39)	2.087	87.81	4.18	3.09	East 2
14	G173.706+02.847	05:41:28.8	+35:47:08	3.65	⋯	0.166	6.98	0.33	⋯	East 1
15	G173.676+02.873	05:41:30.6	+35:49:29	3.39	80.34(0.70)	6.768	284.76	13.5	3.13	East 1

Note. Table contains BGPS source designations, positions, distance from an O9.5V star (D_s), deconvolved effective radius ($R_{\rm eff}$), integrated flux density (S_ν), clump mass (M_g), column density ($N(H_2)$), and self-gravitating pressure ($P_{\rm clump} \approx \pi G\,(M_g/\pi R_{\rm eff}^2)^2$). Clump masses were estimated using the integrated fluxes for a dust temperature = 20 K at a distance of 1.8 kpc. The positions of clumps located near the spherelike shell are highlighted by superscript "†" (see Figure 3 and also the text for more details).

the gas mass is almost same in the present calculations as in the earlier works. More extensive high sensitivity and high resolution observations at mm/sub-mm wavelengths would allow us to further explore the clump mass at the high end of the estimated mass range.

In Figure 3, we show the distribution of clump masses as a function of distance from the location of the O9.5V star. Interestingly, we notice that the clump masses increase as we move away from the location of the ionizing star. This correlation is seen only for those clumps that are distributed near the edges of the spherelike shell (e.g., Central E, East 2, North, and Northwest subregions). The implication of this correlation for the star formation process is discussed in Section 4.

The column densities of clumps can also be computed using the Bolocam data. The column density per beam is given by (see Deharveng et al. 2010):

$$N\,(\mathrm{H_2}) = \frac{S_\nu\, R_t}{\kappa_\nu\, B_\nu(T_d)\, \mu_{\rm H2}\, m_{\rm H}\, \Omega_{\rm beam}}. \quad (2)$$

In the equation above, S_ν, R_t, κ_ν, and $B_\nu(T_d)$ are defined as in Equation (1), $\mu_{\rm H2} = 2.8$ is the mean molecular weight per hydrogen molecule (Kauffmann et al. 2008), the hydrogen atom mass $m_{\rm H}$ is in grams, the beam solid angle $\Omega_{\rm beam}$ ($=\pi\,(\mathrm{FWHM}/(206265 \times \sqrt{4\ln 2}))^2 = 2.9 \times 10^{-8}$ for the Bolocam beam FWHM = 33″) is in steradians, and $N\,(\mathrm{H_2})$ ($= 2.0 \times 10^{22}\, S_\nu(\mathrm{Jy})$ at $T_D = 20$ K; see Bally et al. 2010) is per square centimeter. The column densities thus computed are listed in Table 1. Bolocam clumps have column densities between 0.33×10^{22} and 13.5×10^{22} cm^{-2}.

3.4. IRAC Ratio and H_2 Maps

In order to trace molecular H_2 emission in the complex, we examined the *Spitzer*-IRAC ratio (4.5 μm/3.6 μm) map and the narrow H_2 (2.12 μm) map. The *Spitzer*-IRAC ratio maps have been utilized by many authors to study the interaction between a massive star and its surrounding interstellar medium (ISM) (Povich et al. 2007; Watson et al. 2008; Kumar Dewangan & Anandarao 2010a, 2010b; Dewangan & Anandarao 2011; Dewangan et al. 2012). IRAC 3.6 and 4.5 μm bands have almost identical point response functions (PRFs), therefore, one can directly take the ratio of the 4.5 to 3.6 μm bands. In Figure 4, we display a ratio map of 4.5 μm/3.6 μm emission. The spherical shell-like morphology is evident and the map depicts the edges of the shell. Additionally, several features are

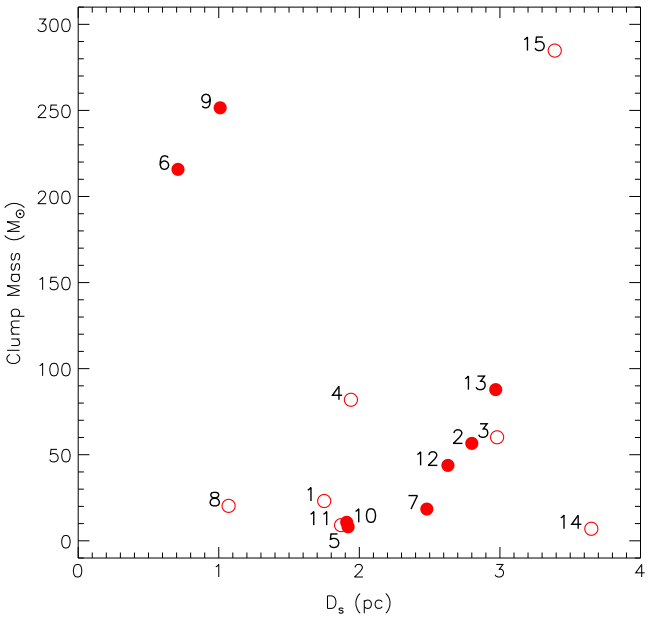

Figure 3. Distribution of clump masses (estimated using Bolocam 1.1 mm data) with respect to the location of an O9.5V star (D_s). Filled circles show the clumps distributed near the edges of the spherelike shell (i.e., Central E, East 2, North, and Northwest subregions; see Figure 2 and Table 1).

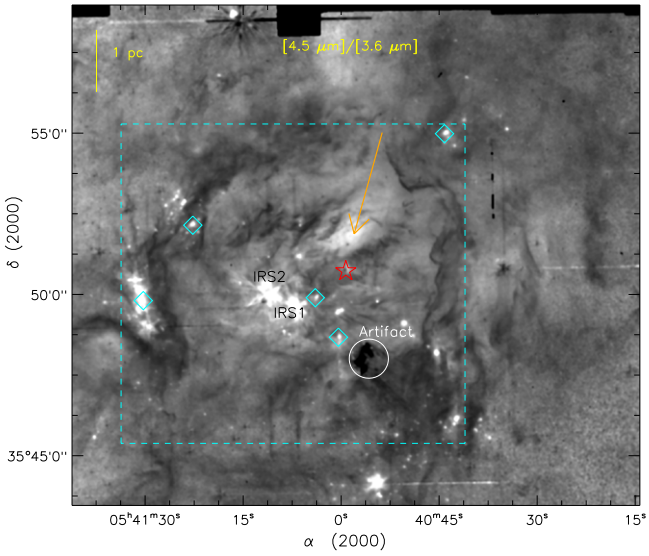

Figure 4. *Spitzer*-IRAC ratio map of 4.5 μm/3.6 μm emission (same area as shown in Figure 1). The area enclosed in the white circle shows an artifact present in the map. The location of an O9.5V star (BD+35°1201) is marked with a star. The diamond symbols indicate the possible outflow activities (see the text for more details). An arrow indicates the bright emission in the map, which probably traces the Brα emission. Note that this bright emission is surrounded by black regions. The dashed box is shown as a zoomed-in view in Figure 5. Two bright sources (i.e., IRS 1 and IRS 2) have sidelobes, therefore the features around these sources in the ratio map cannot be considered for scientific interpretation. The ratio map is subjected to median filtering with a width of 5 pixels and smoothed by 4 pixel × 4 pixel using a boxcar algorithm.

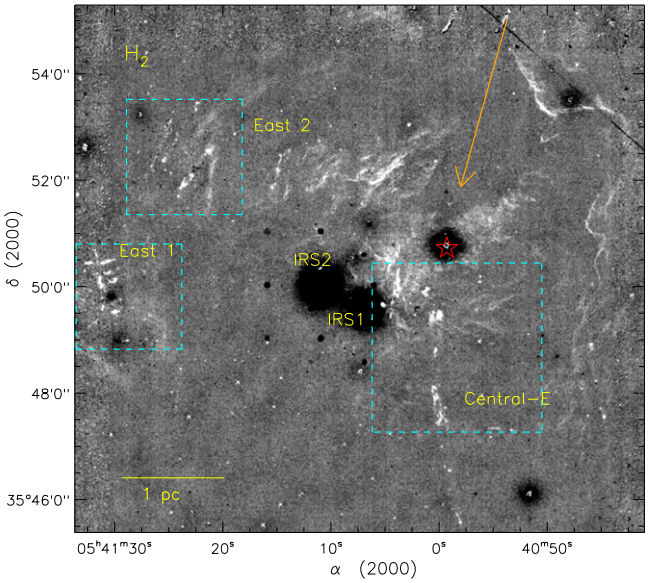

Figure 5. CFHT continuum-subtracted H_2 map (grayscale) at 2.12 μm of the S235 complex (size of the region ~10.′7 × 9.′9 or ~5.6 pc × 5.2 pc), as shown by a dashed box in Figure 4. The location of an O9.5V star (BD+35°1201) is marked with a star symbol. The arrow in orange color is similar to the one shown in Figure 4. The H_2 map is subjected to median filtering with a width of 3 pixels and smoothed by 3 pixel × 3 pixel using a boxcar algorithm to enhance the faint features. The dashed boxes are shown as a zoomed-in view in Figure 6.

seen that are present toward the edges of the shell and in the vicinity of a massive star. In general, the bright emission region in the 4.5 μm/3.6 μm map indicates the excess 4.5 μm emission, while the remaining black or dark gray regions suggest the domination of 3.6 μm emission. The IRAC 4.5 μm band contains a prominent molecular hydrogen line emission (ν = 0–0 $S(9)$; 4.693 μm), which can be excited by outflow shocks, and a hydrogen recombination line Brα (4.05 μm). The IRAC 3.6 μm band harbors PAH emission at 3.3 μm as well as a prominent molecular hydrogen feature at 3.234 μm (ν = 1–0 $O(5)$). In the ratio map, we also notice a bright region in the vicinity of the massive star that coincides with warm dust emission traced at 24 μm as well as with the peak of the radio emission (see the arrow in Figure 4). This bright emission region probably traces the Brα feature originated by photo-ionized gas. In the East 1, East 2, Central E, and Northwest subregions, we found bright emissions that are marked in the ratio map. Note that there are no radio continuum emission detected toward these subregions. Therefore, these emissions are probably H_2 features tracing outflow activities (see Section 3.5 for molecular outflows). Figure 5 shows a continuum-subtracted 2.12 μm H_2 (ν = 1 − 0 S(1)) image, revealing the presence of H_2 emission in the complex. The complex contains diffuse or filamentary-like H_2 features as well as extended H_2 emission. The extended H_2 emission is seen as polar structures (i.e., monopolar, bipolar, and multipolar; see the East 1, East 2, and Central E subregions in Figures 5 and 6). The bipolar emission structure is often interpreted as a bipolar outflow excited by a young star. The multipolar structures could be originated due to the presence of bipolar outflows associated with multiple young stars. The monopolar H_2 structure could be explained by the presence of a bipolar outflow excited by a young star, however, its redshifted component is hidden from view due to inclination angle, extinction, and opacity of the ISM around the young star. In Figure 6, we present H_2, 4.5 μm, and 24 μm images of three subregions (i.e., East 1, East 2, and Central E), where polar structures are traced in the H_2 map. In the East 1 subregion, one multipolar structure is clearly traced. Additionally, some H_2 knots are seen. The H_2 map confirms intense outflow or jet activities in this subregion. The extended 4.5 μm emission is also detected similar to those seen in the H_2 map. The prominent 4.5 μm emission was reported in Paper I using the IRAC ratio map 4.5 μm/8.0 μm (see Figure 11 in Paper I). This subregion contains a cluster of embedded YSOs which makes it difficult to pinpoint the exact exciting source(s) of outflows. However, some probable driving sources (i.e., YSOs) of outflows that are taken from Paper I are marked in the 4.5 and 24 μm images. These highlighted YSOs appear bright in the 24 μm image. In the East 2 subregion, a bipolar structure is detected and is also seen in the 4.5 μm image (also see Figure 12 in Paper I). In Paper I, the driving source of this outflow was characterized as an HMPO candidate. The position of this YSO is also marked in the 4.5 and 24 μm images. The YSO is very bright in the 24 μm image. In the Central E subregion (see Figure 6), we find a bipolar and two monopolar structures (also see source IDs 164 and 165 in Table B2 given in Navarete et al. 2015). The probable exciting sources of one bipolar structure (Outflow-ce1) and one monopolar structure (Jet-ce) are marked in the 4.5 and 24 μm images (see Figure 6). The 24 μm counterparts of these driving sources are also seen. However, the driving source of one monopolar structure (Outflow-ce2; Figure 6) is not detected. In general, one can refer to H_2 nebulosity as an outflow when it traces back to a source. In the present case, considering the morphology of H_2 nebulosity (e.g., Takami et al. 2010), we refer to this

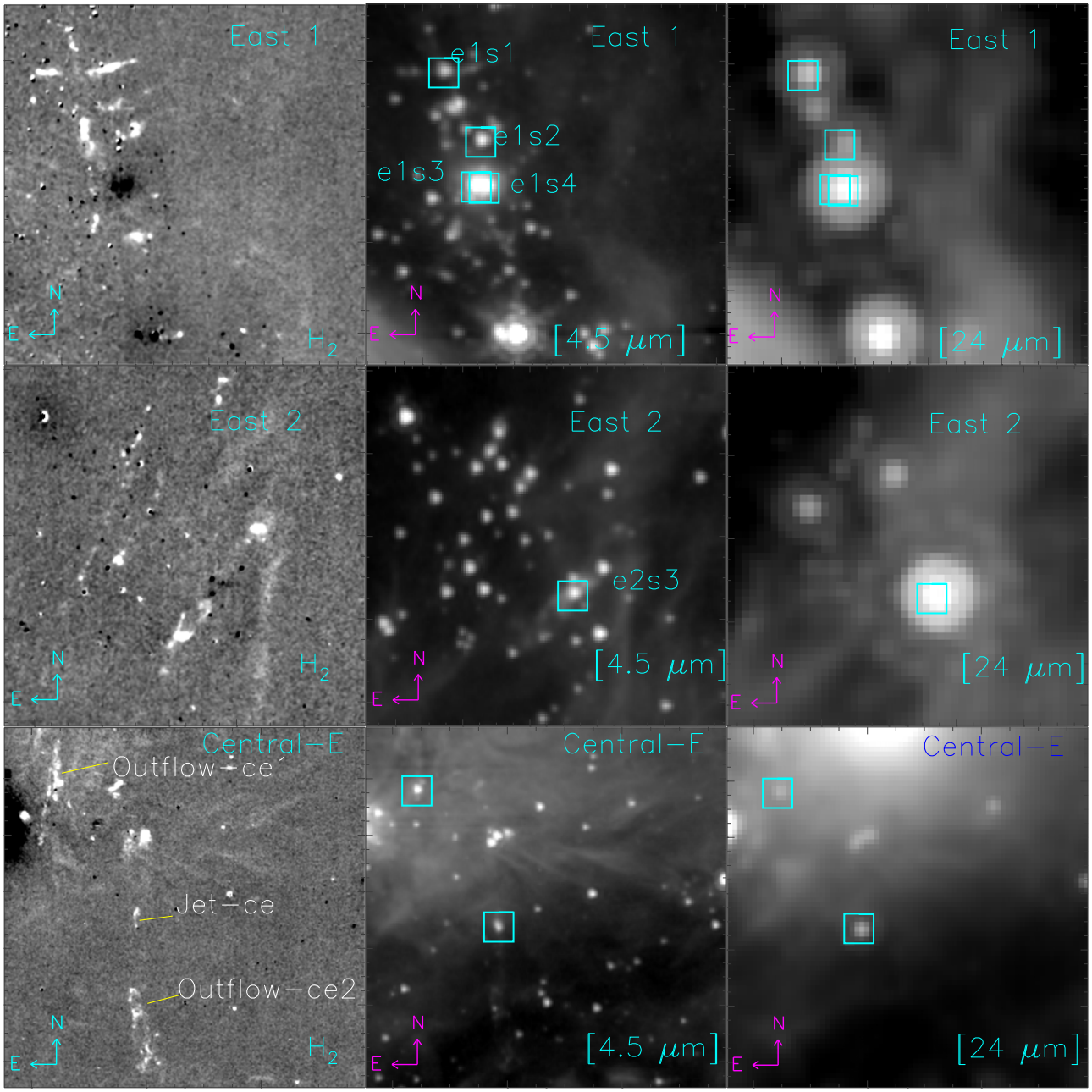

Figure 6. Comparison of H_2, 4.5 μm, and 24 μm images toward three subregions (East 1, East 2, and Central E) in the S235 complex (see dashed boxes in Figure 5). Left panel: CFHT continuum-subtracted H_2 maps (log-scale) at 2.12 μm. Jetlike features and outflows are marked in the figures. The H_2 maps are subjected to median filtering with a width of 3 pixels and smoothed by 3 pixel × 3 pixel using a boxcar algorithm to enhance the faint features. Middle panel: IRAC 4.5 μm images (log-scale). Right panel: MIPS 24 μm images (log-scale). The positions of the probable driving sources of outflows are shown by open squares in both the middle and right panels. Sources are also labeled in East 1 and East 2 subregions in the middle panel.

monopolar structure as the outflow signature. It is generally accepted that the molecular outflows directly indicate the presence of star formation processes. A comparison of the 2.12 μm H_2 emission with the features detected in the ratio map suggest that the black region in the ratio map probably traces the H_2 features (see Figures 4 and 5). However, the presence of a 3.3 μm PAH feature cannot be ignored. The prominent diffuse or filamentary-like H_2 features traced in the H_2 map could be explained by ultraviolet (UV) fluorescence. In summary, the IRAC ratio and H_2 maps trace photodissociation regions (or photon-dominated regions, or PDRs) around the H II region and star formation activities in the complex.

3.5. CO Molecular Gas Associated with the S235 Complex

In the following, we present molecular line data analysis, which enables us to examine the ongoing physical processes and velocity structures present in the complex.

3.5.1. ^{12}CO and ^{13}CO Distributions

In Figure 7, we present the velocity channel maps of the $J = 1-0$ line of ^{13}CO (at intervals of 0.25 km s^{-1}). The maps reveal the distribution of molecular gas components along the line of sight. The maps are shown for the velocity range of -22.75 to -15 km s^{-1}. One may notice from Figure 7 that the

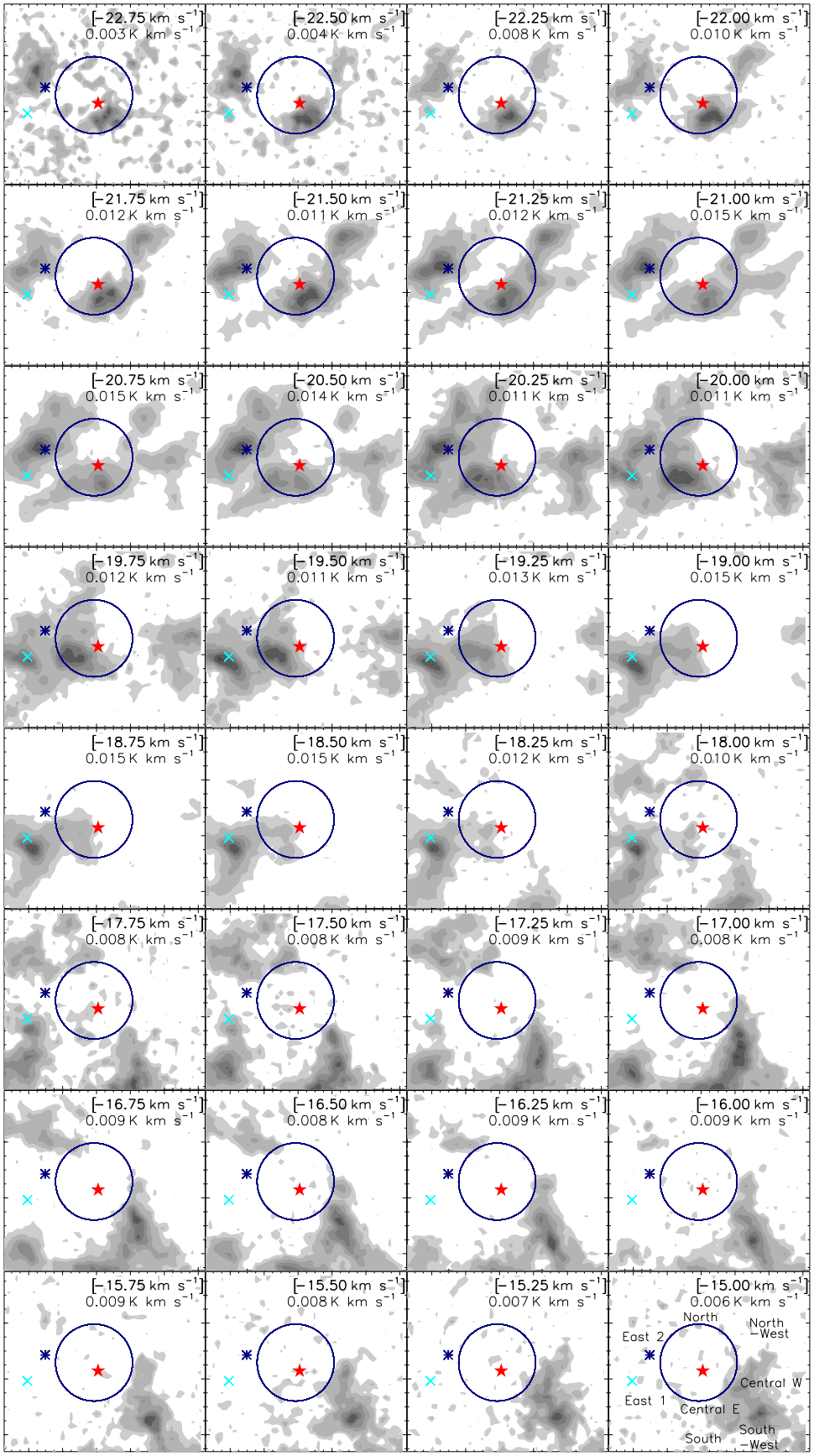

Figure 7. ^{13}CO($J = 1-0$) velocity channel contour maps of the S235 complex. The velocity value (in km s^{-1}) is indicated in each panel. The contour levels are 10%, 20%, 40%, 55%, 70%, 85%, and 98% of the peak value (in K km s^{-1}), which is also given in each panel. The location of an O9.5V star is marked by a filled star. Other marked symbols and labels are similar to those shown in Figure 2(b).

distribution of molecular gas is clumpy, as also previously pointed out by Heyer et al. (1996). In general, the ^{13}CO line is more optically thin compared to the ^{12}CO line. Therefore, the ^{13}CO line data can trace dense condensation and its associated velocity better than ^{12}CO. Considering this fact, we preferred to show only ^{13}CO channel maps of the complex. In the velocity range from −22.75 to −21.25 km s^{-1}, the Central W, East 2, and Northwest subregions are well detected. In the velocity range from −21 to −19.75 km s^{-1}, Central E, Central W, East 1, East 2, North, and Northwest subregions are traced. In the velocity range from −19.50 to −18.0 km s^{-1}, Central E and East 1 subregions are seen. The ^{13}CO gas kinematics presented in this work is consistent with the previous work of Kirsanova et al. (2008). They suggested the presence of three molecular gas components in the complex, which correspond to quiescent undisturbed primordial gas (i.e., $-18\,\mathrm{km\,s^{-1}} < V_{\rm lsr} < -15\,\mathrm{km\,s^{-1}}$ (red)), gas compressed by the shock from expanding S235 H II region (i.e., $-21\,\mathrm{km\,s^{-1}} < V_{\rm lsr} < -18\,\mathrm{km\,s^{-1}}$ (central)), and gas expulsion from the embedded young star clusters driven by the combined effect of the cluster stars (i.e., $-25\,\mathrm{km\,s^{-1}} < V_{\rm lsr} < -21\,\mathrm{km\,s^{-1}}$ (blue)). Furthermore, Kirsanova et al. (2014) utilized NH_3 line data and found the densest molecular clumps associated with East 1, East 2, and Central subregions, mostly belong to the "central" molecular component.

Figure 8 shows the ^{12}CO and ^{13}CO integrated grayscale maps, obtained by integrating over the velocity range between −23 and −18 km s^{-1}. Bolocam dust continuum emission contours are also overlaid on the ^{12}CO integrated map to illustrate the physical association of dust emission with the complex. The integrated CO maps trace a region empty of molecular gas between two subregions, namely North and Northwest. It is to be noted that the region empty of CO gas is exactly coincident with the broken part in the extinction map, where the radio continuum emission at 610 MHz is elongated (see Figures 1(b) and 2(a)). This region also appears to be associated with Brα emission which is surrounded by H_2 and/or PAH features (see Figure 4). It suggests a close interaction between ionized and molecular gas in the complex. It seems that the ionizing photons have managed to escape in this direction. We propose that these features are best explained by the existence of a cavity between the North and Northwest subregions (also see Section 4.1).

In Figure 9, we show position–velocity (p–v) analysis of ^{12}CO and ^{13}CO gas. The p–v plots (R.A.–velocity and decl.–velocity) of ^{12}CO and ^{13}CO gas have revealed noticeable velocity gradients and show essentially the same structure. However, ^{13}CO data provide more information related to the velocity structure of the denser regions compared to ^{12}CO emission (see decl.–velocity plots in Figure 9). The p–v plots of ^{12}CO and ^{13}CO gas reveal an almost semi-ringlike or C-like structure at a larger scale (about 8 pc extended). The detection of such morphology in the p–v plot is often interpreted as the signature of an expanding shell (e.g., Wilson et al. 2005; Arce et al. 2011; Dewangan et al. 2015). We find the expansion velocity of the gas to be ∼3 km s^{-1}. A detailed discussion of this morphology can be found in Section 4.1. Note that the S235 complex hosts the O9.5V type star, therefore the presence of the C-like structure in the complex can be interpreted as caused by the expanding H II region. A similar result was also observed in the W42 star-forming region (see Figure 8 in Dewangan et al. 2015).

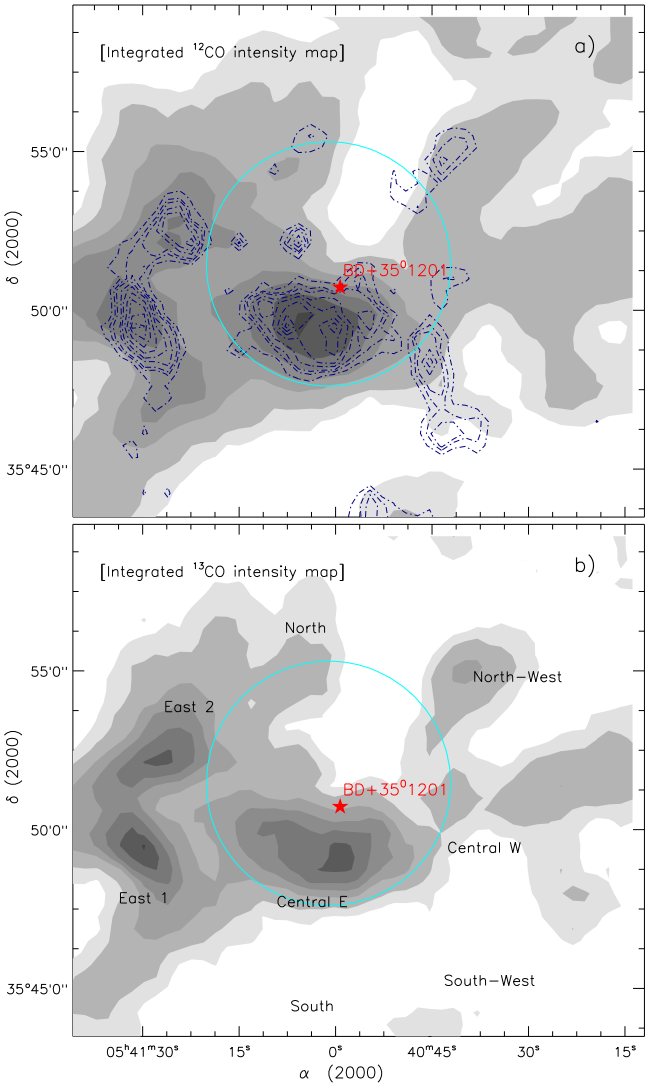

Figure 8. Contour maps of integrated ^{12}CO and ^{13}CO emissions in the velocity range of −23 to −18 km s^{-1}. The contour levels are 10%, 20%, 40%, 55%, 70%, 85%, and 98% of the peak values (i.e., 11.566 K km s^{-1} (^{12}CO) and 31.719 K km s^{-1} (^{13}CO)). In the top panel, Bolocam 1.1 mm dust continuum emission contours are shown by dashed navy contours with levels similar to those shown in Figure 2(b). In both the panels, other marked symbols and labels are similar to those shown in Figure 1.

3.5.2. Molecular Outflows

In addition to the C-like structure in the p–v plots, we have also found noticeable velocity gradients toward the East 1, East 2, Central E, and Northwest subregions, suggesting the presence of outflow activities in each of these subregions. Following Paper I, we know that the East 1, East 2, and Central E subregions contain a cluster of YSOs. We have searched for outflows toward these subregions using the Doppler-shifted velocity components (red, green, and blue). Due to the coarse beam of CO data (beam size ∼46″), we cannot pinpoint the exact exciting source of the outflows in each subregion. Considering this limitation, we have not shown the Doppler-shifted components (red, green, and blue) toward the East 2, Central E, and Northwest subregions. In Figure 10, we present the noticeable receding, approaching, and rest gas components only in East 1 subregion. We have also marked the position of at least one probable driving source of the CO

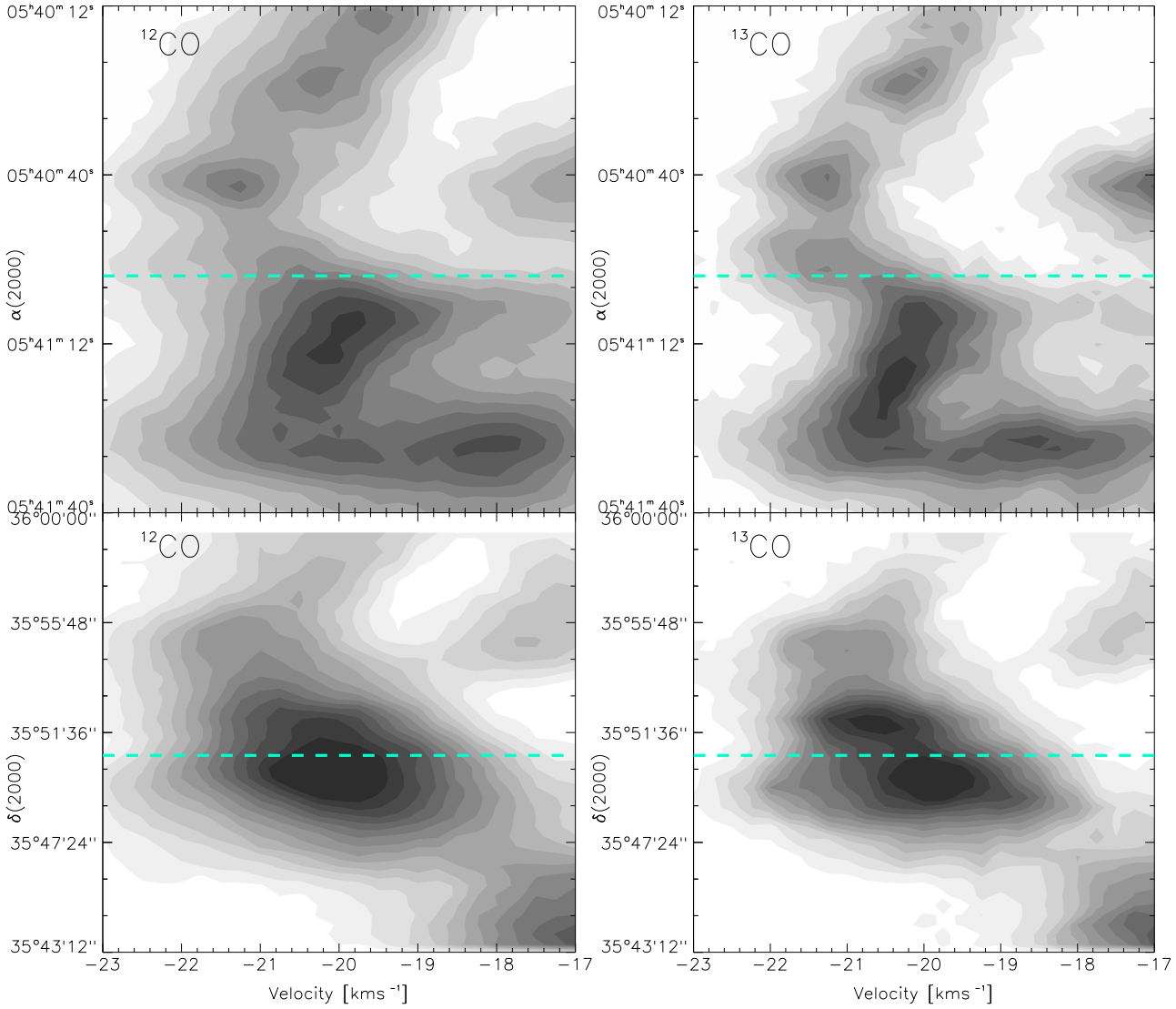

Figure 9. Position–velocity diagrams of ^{12}CO (left) and ^{13}CO (right). Top left: R.A.–velocity map of ^{12}CO. The ^{12}CO emission is integrated over the decl. range from $+35°43'30''$ (35.°725) to $+35°59'13.''2$ (35.°987). The lowest grayscale level corresponds to 30σ (where $1\sigma = 0.01053$ K degree), with successive levels increasing in steps of 30σ. Bottom left: decl.–velocity map of ^{12}CO. The ^{12}CO emission is integrated over the R.A. range from $05^{h}41^{m}40.^{s}8$ (85.°42) to $05^{h}40^{m}12^{s}$ (85.°05). The lowest grayscale level corresponds to 30σ (where $1\sigma = 0.011258$ K degree), with successive levels increasing in steps of 30σ. Top right: R.A.–velocity map of ^{13}CO. The ^{13}CO emission is integrated over the decl. range from $+35°43'30''$ (35.°725) to $+35°59'13.''2$ (35.°987). The lowest grayscale level corresponds to 15σ (where $1\sigma = 0.005265$ K degree), with successive levels increasing in steps of 15σ. Bottom right: decl.–velocity map of ^{13}CO. The ^{13}CO emission is integrated over the R.A. range from $05^{h}41^{m}40.^{s}8$ (85.°42) to $05^{h}40^{m}12^{s}$ (85.°05). The lowest grayscale level corresponds to 15σ (where $1\sigma = 0.005629$ K degree), with successive levels increasing in steps of 15σ. In all the panels, a cyan dashed line shows the location of the ionizing star.

outflow (also see Section 3.4). High resolution molecular line observations are necessary to examine better insight into the molecular outflows in the complex.

3.6. NH_3 Radial Velocity and Non-thermal Velocity Dispersion

As mentioned in the introduction, in general, it is known that NH_3 data trace the densest regions of molecular cloud in a given star-forming region. The properties of densest gas traced by NH_3 line observations have not yet been studied with respect to the ionizing star in the S235 complex. The locations of NH_3 line observations are marked in Figure 2(b), which were mainly observed in the East 1, East 2, and Central E subregions (see Kirsanova et al. 2014 for more details). In Figure 11(a), we show the variation of $NH_3(1,1)$ radial velocity in each subregion as a function of distance from the location of the O9.5V star. The $NH_3(1,1)$ radial velocities vary between -22 and -18.5 km s^{-1} in these three subregions. In general, there are noticeable velocity variations within East 1 (-21.5 to -19.0 km s^{-1}), East 2 (-21.5 to -20.5 km s^{-1}), and Central E (-22 to -18.5 km s^{-1}) subregions. These observational characteristics are also evident in CO data (see Figure 9). Balser et al. (2011) reported the velocity of ionized gas to be about $-25.61(\pm0.12)$ km s^{-1} in the S235 H II region using a hydrogen radio recombination line (H87-93α). Therefore, the molecular gas is redshifted with respect to the ionized gas in the S235 H II region. Interestingly, we note that the radial velocity observed in the Central E subregion shows a linear trend as we move away from the location of a massive star, which is not seen in other two subregions. In each subregion, we have line of sight velocity components and it seems that the radial velocity of gas in the Central E subregion might be almost equal to the real velocity, however, it is not the case for other

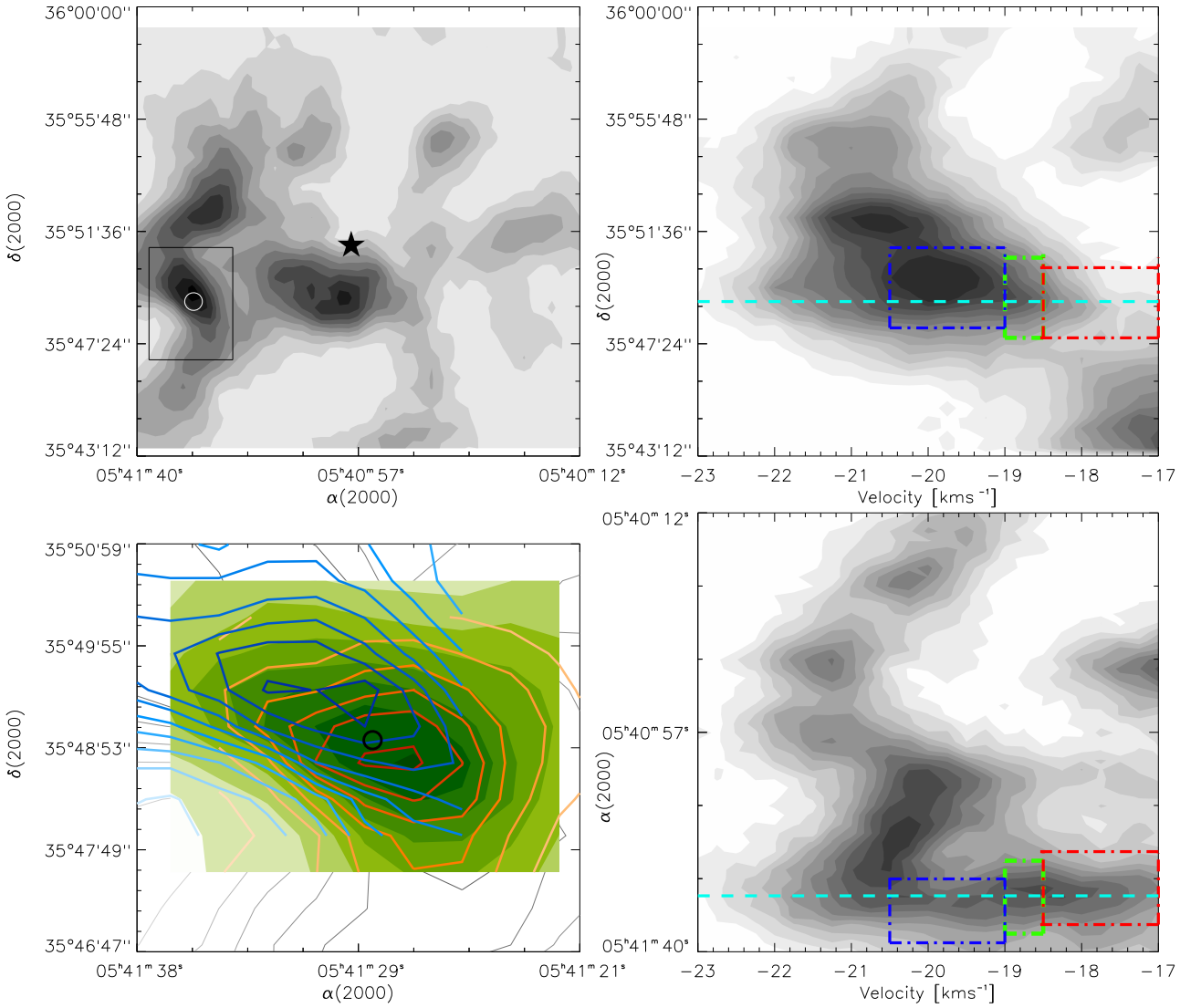

Figure 10. Outflow signature in the East 1 subregion. Top left: a contour map of integrated ^{13}CO emission in the velocity range of −23 to −17 km s^{-1}. The lowest grayscale level represents 20σ, with successive levels increasing in steps of 20σ. The channel rms is 0.159 K km s^{-1}. The solid box in the East 1 subregion is shown as a zoomed-in view in the bottom left panel. The location of an O9.5V star is shown by a filled star. Bottom left: the selected area of contour map (in black color) is highlighted by a box in the top left panel. Different color contours show the receding gas (−18.5 to −17.0 km s^{-1}; red) and approaching gas (−20.5 to −19.0 km s^{-1}; blue) with respect to that at rest (−19.0 to −18.5 km s^{-1}; green). The spatial boundaries of these Doppler components are shown in both the right panels. Top right: decl.–velocity map. Bottom Right: R.A.–velocity map. In both the right panels, the contours are similar to those shown in Figure 9. The slices of receding, approaching, and rest gas are shown in red, blue, and green dashed boxes in both the right panels, respectively. The position of the probable driving source of outflow ($\alpha_{2000} = 05^{h}41^{m}29\overset{s}{.}5$, $\delta_{2000} = +35°48'58\overset{''}{.}7$) is shown by an open circle in both the left panels. The cyan dashed line represents the position of the probable driving source of outflow in both the right panels.

two subregions. The observed trend could be interpreted as the direct influence of the expanding H II region excited by the O9.5V star. Further discussion of this result is presented in Section 4.

We computed thermal sound speed (a_s), non-thermal velocity dispersion (σ_{NT}), and the ratio of thermal to non-thermal pressure ($P_{TNT} = a_s^2/\sigma_{NT}^2$). One can find more details about P_{TNT} in the work of Lada et al. (2003). The sound speed a_s ($=(kT_{kin}/\mu m_H)^{1/2}$) can be estimated with the knowledge of gas kinetic temperature (T_{kin}) and $\mu = 2.37$ (approximately 70% H and 28% He by mass). The non-thermal velocity dispersion is given by:

$$\sigma_{NT} = \sqrt{\frac{\Delta V^2}{8\ln 2} - \frac{kT_{kin}}{17m_H}} = \sqrt{\frac{\Delta V^2}{8\ln 2} - \sigma_T^2}, \quad (3)$$

where ΔV is the measured FWHM line width of the observed NH_3 spectra, σ_T ($=(kT_{kin}/17m_H)^{1/2}$) is the thermal broadening for NH_3 at T_{kin} (e.g., Dunham et al. 2011), and m_H is the mass of hydrogen atom. The computed values of a_s, σ_{NT}, and P_{TNT} are given in Table 2. The value of P_{TNT} is computed for each of the observed positions. In each subregion, the variation of P_{TNT} as a function of distance from the location of a massive star is shown in Figure 11(b). We find an average P_{TNT} value of 0.13, 0.21, and 0.22 for the East 1, East 2, and Central E subregions, respectively. It suggests that non-thermal pressure is dominant in these densest subregions. The lower values of P_{TNT} might be due to contributions from the bipolar outflows, as investigated in previous section. The average values of Mach numbers (σ_{NT}/a_s) estimated for the East 1, East 2, and Central E

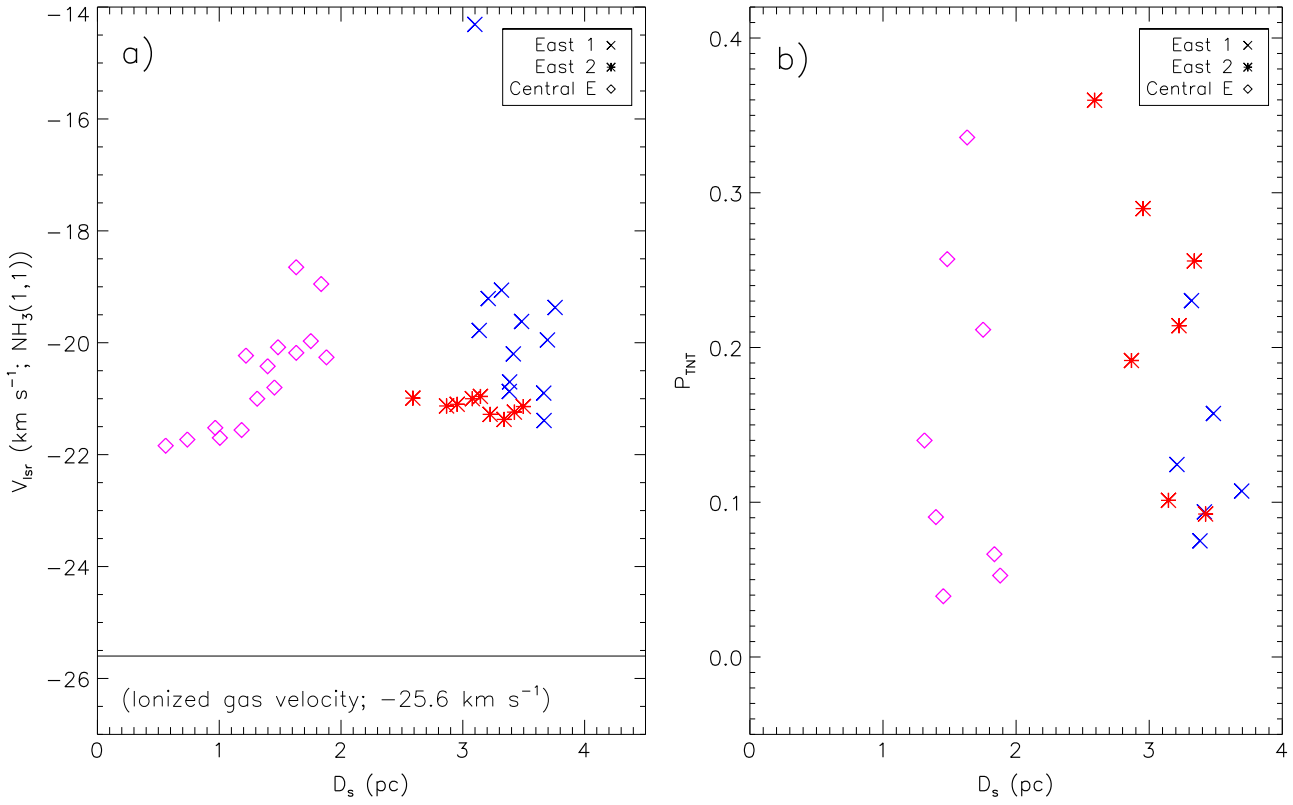

Figure 11. (a) Variation of $NH_3(1,1)$ radial velocity (V_{lsr}) in each subregion as a function of distance from the location of an O9.5V star (D_s) (see Figure 2(b) and Table 2). (b) Ratio of thermal to non-thermal gas pressure ($P_{TNT} = a_s^2/\sigma_{NT}^2$) vs. D_s (see Table 2). The low value of P_{TNT} corresponds to the dominant term in the denominator (i.e., non-thermal velocity dispersion (σ_{NT})).

subregions are 2.9, 2.3, and 2.9, respectively, which indicates that these subregions are supersonic.

3.7. Feedback of a Massive Star

In this section, we derive the various pressure components (pressure of an H II region ($P_{H\,II}$), radiation pressure (P_{rad}), and stellar wind ram pressure (P_{wind})) driven by a massive star to study its feedback in the vicinity.

It is found that the massive star is approximately located at the center of the spherelike shell. The radio continuum images presented in this work can be used to estimate the number of Lyman continuum photons (N_{uv}). The expression of N_{uv} is given by (Matsakis et al. 1976)

$$N_{uv}(s^{-1}) = 7.5 \times 10^{46} \left(\frac{S_\nu}{\mathrm{Jy}}\right)\left(\frac{D}{\mathrm{kpc}}\right)^2 \left(\frac{T_e}{10^4\ \mathrm{K}}\right)^{-0.45} \times \left(\frac{\nu}{\mathrm{GHz}}\right)^{0.1}, \quad (4)$$

where S_ν is the measured total flux density in Jy, D is the distance in kpc, T_e is the electron temperature, and ν is the frequency in GHz. The calculation of N_{uv} is performed for both the radio frequencies (0.61 GHz and 1.4 GHz) separately. Substituting $D = 1.8$ kpc, $T_e = 10{,}000$ K, and $S_{1.4} = 1.92$ Jy, we compute $N_{uv} = 4.9 \times 10^{47}\ s^{-1}$. Similarly, we find $N_{uv} = 8.2 \times 10^{47}\ s^{-1}$ for D, T_e, and $S_{0.61} = 3.49$ Jy. The estimates of ionizing photon flux values at different frequencies correspond to a single ionizing star of O9.5V spectral type (Martins et al. 2005), which is also in agreement with the previously reported spectral type of the ionizing source of the complex (e.g., Georgelin et al. 1973).

The different pressure components ($P_{H\,II}$, P_{rad}, and P_{wind}; as mentioned above) are defined as below (e.g., Bressert et al. 2012):

$$P_{H\,II} = \mu m_H c_s^2 \left(\sqrt{\frac{3N_{uv}}{4\pi\ \alpha_B\ D_s^3}}\right); \quad (5)$$

$$P_{rad} = L_{bol}/4\pi c D_s^2; \quad (6)$$

$$P_{wind} = \dot{M}_w V_w / 4\pi D_s^2. \quad (7)$$

In the equations above, N_{uv}, μ, and m_H are defined earlier, the radiative recombination coefficient is "α_B" ($=2.6 \times 10^{-13} \times (10^4\ \mathrm{K}/T_e)^{0.7}\ \mathrm{cm^3\ s^{-1}}$; see Kwan 1997), c_s is the sound speed in the photoionized region ($=10$ km s^{-1}), $\dot{M}_w$ is the mass-loss rate, V_w is the wind velocity of the ionizing source, L_{bol} is the bolometric luminosity of the complex, and D_s is the projected distance from the location of the O9.5V type star to the subregions where the pressure components are estimated. One can infer from Equations (5)–(7) that the pressures, P_{rad} and P_{wind}, scale as D_s^{-2} while $P_{H\,II}$ scales as $D_s^{-3/2}$.

Note that the highlighted subregions are not located at the same projected distance from the location of a massive star (see Figures 2 and 3). Therefore, we compute the pressure components driven by a massive star (i.e., $P_{H\,II}$, P_{rad}, and P_{wind}) at D_s = 3.4 pc (East 1), 3.0 pc (East 2), 1.5 pc

Table 2
Physical Parameters Derived from NH_3 Line Data (from Kirsanova et al. 2014)

Region	R.A. [2000]	Decl. [2000]	D_s (pc)	T_{kin} (K)	$n(H_2)$ (10^3 cm^{-3})	ΔV (km s^{-1})	V_{lsr} (km s^{-1})	a_s (km s^{-1})	σ_T (km s^{-1})	σ_{NT} (km s^{-1})	P_{TNT} (a_s^2/σ_{NT}^2)
e1	5:41:33.8	+35:51:07	3.67	⋯	⋯	2.14	−21.39	⋯	⋯	⋯	⋯
e1	5:41:33.8	+35:50:27	3.66	⋯	⋯	2.34	−20.90	⋯	⋯	⋯	⋯
e1	5:41:33.8	+35:49:47	3.70	21.20	⋯	1.95	−19.95	0.27	0.10	0.82	0.11
e1	5:41:33.8	+35:49:07	3.76	⋯	⋯	1.52	−19.37	⋯	⋯	⋯	⋯
e1	5:41:31.1	+35:51:07	3.38	⋯	⋯	1.06	−20.70	⋯	⋯	⋯	⋯
e1	5:41:31.1	+35:50:27	3.38	20.73	18	2.30	−20.87	0.27	0.10	0.97	0.08
e1	5:41:31.1	+35:49:47	3.41	18.57	19	1.95	−20.20	0.25	0.09	0.82	0.09
e1	5:41:31.1	+35:49:07	3.48	31.53	19	1.97	−19.62	0.33	0.12	0.83	0.16
e1	5:41:28.4	+35:50:27	3.10	⋯	⋯	2.69	−14.31	⋯	⋯	⋯	⋯
e1	5:41:28.4	+35:49:47	3.14	⋯	⋯	1.54	−19.78	⋯	⋯	⋯	⋯
e1	5:41:28.4	+35:49:07	3.21	19.31	13	1.73	−19.21	0.26	0.10	0.73	0.12
e1	5:41:28.4	+35:48:27	3.32	18.99	⋯	1.27	−19.06	0.25	0.10	0.53	0.23
e2	5:41:31.1	+35:52:27	3.50	⋯	⋯	1.68	−21.14	⋯	⋯	⋯	⋯
e2	5:41:31.1	+35:51:47	3.42	17.56	⋯	1.91	−21.24	0.24	0.09	0.81	0.09
e2	5:41:28.4	+35:51:47	3.14	16.69	⋯	1.78	−20.96	0.24	0.09	0.75	0.10
e2	5:41:28.4	+35:52:27	3.22	17.69	⋯	1.27	−21.28	0.25	0.09	0.53	0.21
e2	5:41:28.4	+35:53:07	3.34	28.56	3	1.48	−21.37	0.31	0.12	0.62	0.26
e2	5:41:25.8	+35:51:47	2.87	17.68	⋯	1.34	−21.13	0.25	0.09	0.56	0.19
e2	5:41:25.8	+35:52:27	2.95	20.81	⋯	1.19	−21.10	0.27	0.10	0.50	0.29
e2	5:41:25.8	+35:53:07	3.08	⋯	⋯	1.47	−21.00	⋯	⋯	⋯	⋯
e2	5:41:23.1	+35:51:47	2.59	36.45	⋯	1.42	−20.99	0.35	0.13	0.59	0.36
cn	5:41:15.1	+35:49:47	1.75	22.48	⋯	1.44	−19.97	0.28	0.10	0.60	0.21
cn	5:41:15.1	+35:49:07	1.88	22.25	1	2.84	−20.26	0.28	0.10	1.20	0.05
cn	5:41:12.4	+35:49:47	1.48	27.92	4	1.46	−20.08	0.31	0.12	0.61	0.26
cn	5:41:12.4	+35:49:07	1.63	21.61	6	1.13	−20.18	0.27	0.10	0.47	0.34
cn	5:41:12.4	+35:48:27	1.84	14.32	⋯	2.03	−18.95	0.22	0.08	0.86	0.07
cn	5:41:09.8	+35:49:47	1.22	⋯	⋯	2.41	−20.23	⋯	⋯	⋯	⋯
cn	5:41:09.8	+35:49:07	1.40	23.65	⋯	2.24	−20.42	0.28	0.11	0.95	0.09
cn	5:41:09.8	+35:48:27	1.63	⋯	⋯	0.82	−18.65	⋯	⋯	⋯	⋯
cn	5:41:07.1	+35:49:47	0.97	⋯	⋯	3.06	−21.52	⋯	⋯	⋯	⋯
cn	5:41:07.1	+35:49:07	1.18	⋯	⋯	1.66	−21.56	⋯	⋯	⋯	⋯
cn	5:41:07.1	+35:48:27	1.45	13.41	5	2.55	−20.80	0.21	0.08	1.08	0.04
cn	5:41:04.4	+35:49:47	0.74	⋯	⋯	1.54	−21.73	⋯	⋯	⋯	⋯
cn	5:41:04.4	+35:49:07	1.01	⋯	⋯	1.87	−21.70	⋯	⋯	⋯	⋯
cn	5:41:04.4	+35:48:27	1.31	15.44	2	1.46	−21.00	0.23	0.09	0.61	0.14
cn	5:41:01.8	+35:49:47	0.56	43.04	5	1.07	−21.84	0.38	0.14	0.43	0.79

Note. Table contains information about three subregions (e1 = East 1, e2 = East 2, and cn = Central E), positions, distance from an O9.5V star (D_s), kinematical temperature (T_{kin}), volume density ($n(H_2)$), NH_3 (1,1) line width (ΔV), NH_3 (1,1) line velocity (V_{lsr}), sound speed (a_s), thermal velocity dispersion (σ_T), non-thermal velocity dispersion (σ_{NT}), and ratio of thermal to non-thermal gas pressure ($P_{TNT} = a_s^2/\sigma_{NT}^2$) (see the text for more details and also Figures 2(b) and 11).

(Central E), 2.6 pc (North), 2.7 pc (Northwest), 1.9 pc (Central W), and 3.0 pc (Southwest) (see Figures 2 and 3).

Evans & Blair (1981) estimated a total gas mass of the S235 cloud to be about 3000 $M_\odot$ in a radius of 3 pc. Nordh et al. (1984) computed a total luminosity of S235 of $\sim 8 \times 10^4\, L_\odot$. We use $M_{cloud} \approx 3000\, M_\odot$, $R_c \approx 3.0$ pc, $L_{bol} \approx 8 \times 10^4\, L_\odot$, $\dot{M}_w \approx 1.58 \times 10^{-9}\, M_\odot\, yr^{-1}$ (for O9.5V star; Marcolino et al. 2009), $V_w \approx 1500$ km s^{-1} (for O9.5V star; Marcolino et al. 2009) in the above equations to compute the pressure contributions driven by a massive star on different subregions (see the list in Table 3). The error associated with each pressure component related to each subregion is also given in Table 3. In the S235 complex, we find that the pressure of the H II region exceeds the radiation pressure and the stellar wind pressure (see Table 3). The total pressure ($P_{total} = P_{H\,II} + P_{rad} + P_{wind}$) driven by a massive star on each subregion is also tabulated in Table 3, which is found to be $\sim 10^{-10}$ dynes cm^{-2} for each subregion.

Additionally, pressure exerted by the self-gravity of the surrounding molecular gas is also estimated using the relation (e.g., Harper-Clark & Murray 2009)

$$P_{cloud} \approx \pi G \Sigma^2, \quad (8)$$

where Σ ($=M_{cloud}/\pi R_c^2$) is the mean mass surface density of the cloud, M_{cloud} is the mass of the molecular gas, and R_c is the radius of the molecular region. The value of P_{cloud} for the entire cloud is estimated to be $\sim(1.0 \pm 0.5) \times 10^{-10}$ dynes cm^{-2}. The values of P_{cloud} associated with different subregions are also found to be $\sim$0.1–3.0 $\times 10^{-10}$ dynes cm^{-2} (see Table 1 and Figure 2(a)). In subregions, we find $P_{total} \gtrsim P_{cloud}$ (see Table 3). This argument is still valid if we put all the subregions at the same projected distance (i.e., $D_s = 3.0$ pc; see pressure calculations related to East 2 in Table 3). Additionally, the P_{cloud} is relatively higher than the pressure associated with a typical cool molecular cloud ($\sim 10^{-11}$–10^{-12} dynes cm^{-2} for a temperature $\sim$20 K and the particle density $\sim 10^3$–10^4 cm^{-3}) (see Table 7.3 of Dyson & Williams 1980). Considering the pressure value associated with a typical cool molecular cloud, we infer that an additional physical process has been acted to

Table 3
Pressure Components Driven by an O9.5V Star on Different Subregions of the S235 Complex

Pressure (dynes cm^{-2})	East 1 at $D_s = 3.4$ pc	East 2 at $D_s = 3.0$ pc	Central E at $D_s = 1.5$ pc	North at $D_s = 2.6$ pc	Northwest at $D_s = 2.7$ pc	Central W at $D_s = 1.9$ pc	Southwest at $D_s = 3.0$ pc
$P_{\rm H\ II}$	$(7.8 \pm 0.2) \times 10^{-11}$	$(9.4 \pm 0.2) \times 10^{-11}$	$(2.7 \pm 0.07) \times 10^{-10}$	$(1.2 \pm 0.03) \times 10^{-10}$	$(1.1 \pm 0.03) \times 10^{-10}$	$(1.9 \pm 0.05) \times 10^{-10}$	$(9.4 \pm 0.2) \times 10^{-11}$
$P_{\rm rad}$	$(7.4 \pm 0.2) \times 10^{-12}$	$(9.5 \pm 0.5) \times 10^{-12}$	$(3.8 \pm 0.2) \times 10^{-11}$	$(1.3 \pm 0.06) \times 10^{-11}$	$(1.2 \pm 0.06) \times 10^{-11}$	$(2.4 \pm 0.1) \times 10^{-11}$	$(9.5 \pm 0.5) \times 10^{-12}$
$P_{\rm wind}$	$(1.1 \pm 0.08) \times 10^{-14}$	$(1.4 \pm 0.1) \times 10^{-14}$	$(5.6 \pm 0.4) \times 10^{-14}$	$(1.9 \pm 0.1) \times 10^{-14}$	$(1.7 \pm 0.1) \times 10^{-14}$	$(3.5 \pm 0.2) \times 10^{-14}$	$(1.4 \pm 0.1) \times 10^{-14}$
$P_{\rm total}$	$(0.9 \pm 0.02) \times 10^{-10}$	$(1.0 \pm 0.02) \times 10^{-10}$	$(3.0 \pm 0.07) \times 10^{-10}$	$(1.3 \pm 0.03) \times 10^{-10}$	$(1.2 \pm 0.03) \times 10^{-10}$	$(2.1 \pm 0.05) \times 10^{-10}$	$(1.0 \pm 0.02) \times 10^{-10}$

Note. The pressure exerted by the self-gravitating molecular cloud in each subregion is estimated to be ≈ 0.1–3.0×10^{-10} dynes cm^{-2} (see text for more details).

compress the surrounding molecular gas to enhance the pressure in the complex. Consequently, this process may stimulate the initial collapse and fragmentation of the extended molecular cloud. The pressure calculations indicate that the photoionized gas can be considered as the important contributor for the feedback mechanism in the S235 complex.

3.8. YSOs in S235

3.8.1. Identification of YSOs

A population of YSOs can be identified using NIR and MIR color schemes as utilized by many authors (e.g., Allen et al. 2004; Lada et al. 2006; Gutermuth et al. 2009). In Paper I, we identified YSOs using only IRAC data. In the present work, we also employed the UKIDSS-GPS NIR data, in combination with IRAC data for finding more deeply embedded and faint sources. Note that the UKIDSS-GPS NIR data are three magnitudes deeper than 2MASS. Here, we describe the procedure of YSOs identification and classification using photometric IRAC and GPS data.

1. We selected sources having detections in all four *Spitzer*-IRAC bands, which were taken from Paper I. We found 131 YSOs (52 Class I and 79 Class II), 4 Class III, 133 photospheres, and 38 contaminants in our selected region shown in Figure 1(a). The details of YSO classification can be found in Paper I. Figure 12(a) displays the different selected sources. In Figure 12(a), we show Class I YSOs (red circles), Class II YSOs (open blue triangles), Class III YSOs (black squares), photospheric emissions (gray dots), and PAH-emission-contaminated apertures (magenta multiplication symbols).
2. Then, we considered sources lacking detections in two longer wavelengths of IRAC bands (5.8 and 8.0 μm). For such sources, the GPS-IRAC (H, K, 3.6, and 4.5 μm) classification scheme was utilized, as described in detail by Gutermuth et al. (2009). In this method, the dereddened color–color space ($[K-[3.6]]_0$ and $[[3.6]-[4.5]]_0$) was used to identify infrared excess sources. These dereddened colors were computed using the color excess ratios given in Flaherty et al. (2007). This scheme also offered to identify possible dim extragalactic contaminants from YSOs with additional conditions (i.e., $[3.6]_0 < 15$ mag for Class I and $[3.6]_0 < 14.5$ mag for Class II). We used the observed color and the reddening law (from Flaherty et al. 2007) to compute the dereddened 3.6 μm magnitudes. In the end, 16 Class I and 133 Class II YSOs were obtained using GPS-IRAC data (see Figure 12(b).
3. The NIR color–color diagram ($H-K$ versus $J-H$) is a very useful tool to select infrared excess sources. We applied this scheme for sources having detections in all three *JHK* bands. Figure 12(c) shows an NIR color–color diagram of such sources. The reddening lines are drawn using the extinction law of Indebetouw et al. (2005). The color–color diagram is divided into three different regions, namely "I," "II," and "III." One can find more details about NIR YSO classification in Sugitani et al. (2002) and Dewangan et al. (2012). The sources distributed in the "I" region represent the likely Class I objects (protostellar objects). T Tauri-like sources (Class II objects) are identified within the "II" region along the T Tauri locus with large NIR excess. The sources that fall between the reddening bands of the main-sequence and giant stars are located in the "III" region. With this method, we obtained 5 Class I and 96 Class II sources (see Figure 12(c)).
4. Finally, we considered sources (significant in number) that had detections only in the *H* and *K* bands. In order to further identify infrared excess sources from such a sample, we utilized a color–magnitude ($H-K/K$) diagram (see Figure 12(d)). The diagram allowed us to select red sources having $H-K > 1.04$. The color–magnitude analysis of the nearby control field allowed us to infer this color criterion. This condition provided us with 54 additional deeply embedded infrared excess sources.

Recently, Chavarría et al. (2014) also presented photometry of the entire extended star-forming S235 region (including the S235AB region) using NIR and *Spitzer* data. These authors obtained *K*-band observations using the 2.1 m telescope located at Kitt Peak National Observatory. Additionally, they observed *J* and *H* bands using the 6.5 m Multiple Mirror Telescope (MMT) telescope located at Fred Lawrence Whipple Observatory. They identified 690 YSOs in the entire S235 complex. However, they did not separate the contaminations in their analysis. Additionally, they did not provide the positions of their identified YSOs. Therefore, a comparison of our selected YSOs to the sources identified by Chavarría et al. (2014) cannot be thoroughly performed in this work (see Figure 13 in this work and Figure B2 in Chavarría et al. 2014). In our YSO analysis, we have carefully separated the contaminations from YSO populations. As a result of the four schemes explained above, a total of 435 YSOs were identified in the complex (the S235AB region is not included). The positions of all YSOs are shown in Figure 13.

3.8.2. Spatial Distribution of YSOs

In recent years, the surface density of young stellar populations in star-forming regions has been adopted to identify and to study the young stellar clusters (e.g., Gutermuth et al. 2009; Bressert et al. 2010). In Paper I, the surface density map of YSOs was computed using the nearest-neighbor (NN) technique (also see Gutermuth et al. 2009; Bressert et al. 2010, for more details). Here, we also followed the same procedure and generated the surface density map of all the selected 435 YSOs. The map was created using a 5″ grid and six NN at a distance of 1.8 kpc. Figure 13 shows the resultant surface density contours of YSOs overlaid on the extinction map. The contour levels are shown at 10, 20, 40, and 70 YSOs pc^{-2}, increasing from the outer to the inner regions. The figure clearly illustrates the spatial correlation between YSOs surface density and extinction.

The surface density analysis allows us to trace the individual groups or clusters of YSOs. We want to identify the clustered populations from distributed sources. However, there is no unique method to find a cutoff distance for tracing these two populations. Statistical analysis, such as empirical cumulative distribution (ECD) of YSOs as a function of NN distance, is often studied to infer the clustered YSO populations in star-forming regions (see Chavarría et al. 2008; Gutermuth et al. 2009; Dewangan & Anandarao 2011, for more details). In the ECD analysis, a cutoff length (also referred to as the distance of inflection d_c) is chosen, to delineate the low-

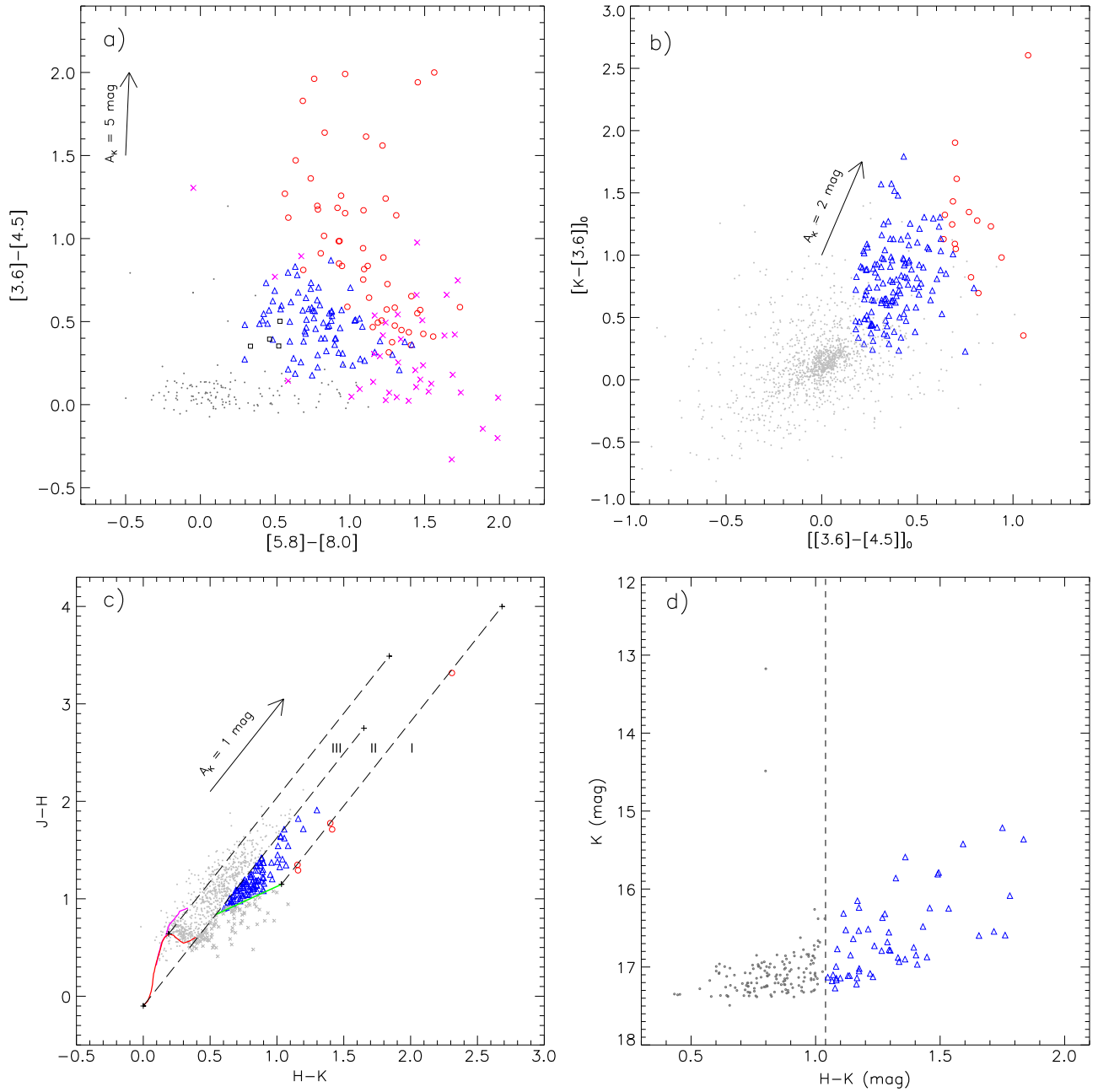

Figure 12. (a) *Spitzer*-IRAC color–color diagram ([3.6]−[4.5] vs. [5.8]−[8.0]) (from Dewangan & Anandarao 2011). The "□" and "×" symbols indicate the Class III sources and identified PAH-emission-contaminated apertures, respectively. (b) The dereddened $[K-[3.6]]_0$ vs. $[[3.6]-[4.5]]_0$ color–color diagram using GPS and IRAC data. (c) NIR color–color diagram ($H-K$ vs. $J-H$). The solid curves show the unreddened locus of main-sequence stars (red) and giants (magenta) (from Bessell & Brett 1988). Classical T Tauri (CTTS) locus (in the California Institute of Technology (CIT) system; Meyer et al. 1997) is drawn with a solid green line. The three parallel long-dashed lines represent the reddening vectors (with $A_K = 3$ mag) of giants, main-sequence stars, and CTTS stars. The extinction vector $A_K = 1$ mag is also shown in the diagram. The extinction vectors are drawn from Indebetouw et al. (2005) extinction laws. The color–color diagram is divided into three different subregions, namely "I," "II," and "III." The loci of the unreddened dwarf (Bessell & Brett (BB) system), giant (BB-system) and CTTS (CIT system) are transferred into the 2MASS system using transformation equations given in Carpenter (2001). (d) Color–magnitude diagram ($H-K/K$) of the sources detected in the H and K bands. In all the panels, we show Class I (red circles) and Class II (open blue triangles) YSOs. In the first two panels, the arrow represents the extinction vector corresponding to the average extinction laws from Flaherty et al. (2007). The dots (in gray color) show the stars with only photospheric emissions (see the text for YSO selection conditions).

density/distributed populations. For the present case, we selected a cutoff distance of $d_c \sim 52''$ (0.45 pc at a distance of 1.8 kpc), which separates the cluster members within the contour level of 10 YSOs pc^{-2}. Such a cutoff distance has been determined for different star-forming regions such as the Diamond Ring region in the Cygnus-X star-forming complex ($d_c \sim 61''$ or 0.43 pc at 1450 pc; Beerer et al. 2010), the Cygnus-OB2 region in the Cygnus-X complex ($d_c \sim 72''$ or 0.51 pc; Guarcello et al. 2013), and the W5 star-forming region ($d_c \sim 33''$ or 0.32 pc at 2 kpc; Chavarría et al. 2014). The comparison of d_c values suggests that W5 is more densely populated with YSOs compared to Cygnus-X. In general, the value of d_c offers the most densely YSO-populated star-forming regions. The ECD analysis yielded a clustered fraction

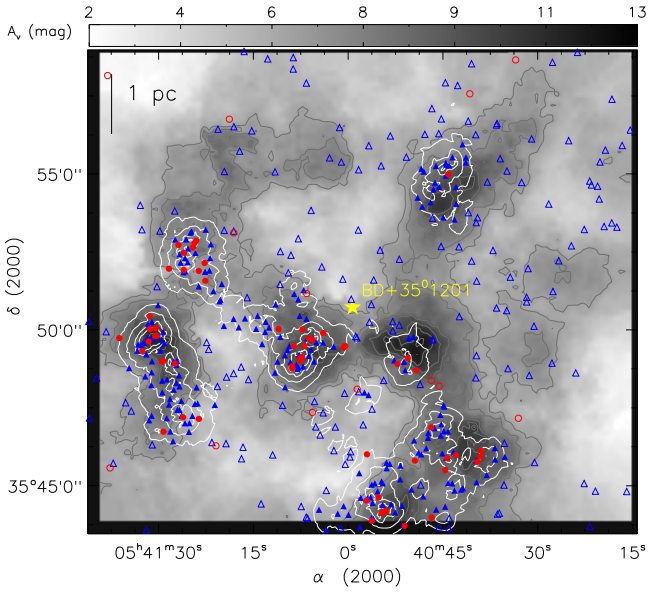

Figure 13. Overlay of YSO surface density contours on the extinction map. The background map is similar to the one shown in Figure 2(a). The surface density contours (in white color) are shown at 10, 20, 40, and 70 YSOs pc^{-2}, increasing from the outer to the inner regions. The positions of Class I and Class II YSOs identified within our selected region are shown by red circles and blue triangles, respectively. All the cluster members (YSOs having $d_c \leqslant 0.453$ pc) are shown by filled symbols (see text for details). The YSOs greater than d_c (>0.453 pc) are marked by open symbols. The location of an O9.5V star is shown by a filled star.

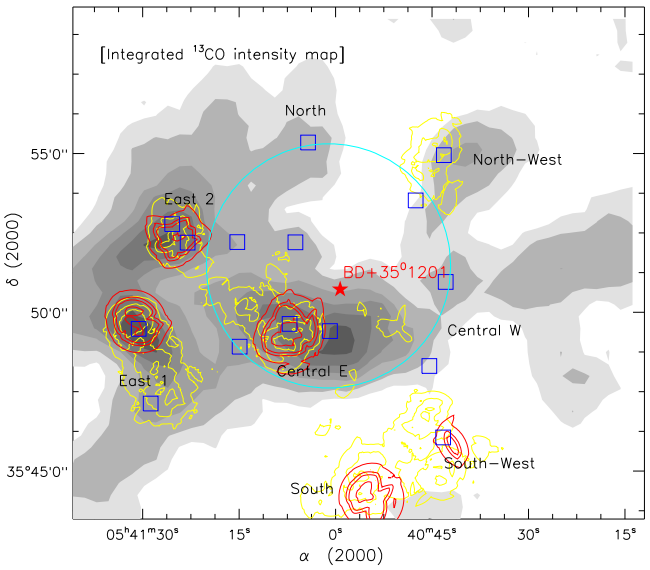

Figure 14. Overlay of Class I and Class II YSO surface density contours on the integrated ^{13}CO map. The background map is similar to the one shown in Figure 8(b). The surface density contours of Class I YSOs are drawn in red color with 5, 8, 10, and 20 YSO pc^{-2}. The Class II YSO surface density contours are overlaid in yellow color with 10, 20, and 40 YSO pc^{-2}. The location of an O9.5V star is shown by a filled star. The positions of dust clumps are shown by blue squares in the map (see Table 1).

of about 59% YSOs (i.e., 258 from a total of 435 YSOs). The YSO clusters are mainly distributed in the East 1, East 2, Central E, Central W, Northwest, South, and Southwest subregions. In the Central E and East 1 subregions, we found the highest level of surface density contours. The North subregion is not associated with any YSO cluster; however, it contains a few Class II YSOs. The clustered and scattered YSO locations are identified in Figure 13 by filled and open symbols, respectively.

We also constructed separately the surface density contour maps of Class I and Class II YSOs, using the same algorithm as explained above. The surface density contour maps of Class I and Class II YSOs are shown in Figure 14(a). The surface density of Class I YSOs lies between 0.04 and 42.75 YSOs pc^{-2} with a dispersion (σ) of 2.64 and is shown by contour levels of 5, 8, 10, and 20 YSOs pc^{-2}. Similarly, the surface density of Class II YSOs is found to lie between 0.17 and 174 YSOs pc^{-2}, with a dispersion of 6.62 and is drawn at contour levels of 10, 20, and 40 YSOs pc^{-2}. All the Class I and Class II YSO clusters are exclusively found in the regions with $A_V > 8$ mag. The Class I YSO clusters are traced in the East 1, East 2, Central E, South, and Southwest subregions (see Figure 14(a)).

4. DISCUSSION

4.1. Expanding H II Region

One of the important results of the present work is the identification of an almost semi-ringlike or C-like structure in the *p–v* plots, which is similar to the one observed in the Orion nebula (see Figure 10(b) in Wilson et al. 2005) and to that in W42 (see Figure 8 in Dewangan et al. 2015). Arce et al. (2011) also studied such observed structures in the Perseus molecular cloud along with the modeling of expanding bubbles in a turbulent medium. These authors suggested that the semi-ringlike or C-like structure in the *p–v* plots is the signature of an expanding shell. They also mentioned that the ringlike morphology can be seen in the *p–v* plot when the powerful ionizing source is situated at the center of the region. Additionally, the NH_3 radial velocity observed in the Central E subregion exhibits a linear trend as one moves away from the location of a massive star. The analysis of pressure contributions driven by a massive star (i.e., $P_{\rm H\,II}$, $P_{\rm rad}$, and $P_{\rm wind}$) indicates that the $P_{\rm H\,II}$ value is higher than the other pressure components. Therefore, it seems that the C-like structure in the *p–v* plots corresponds to the expanding H II region excited by the O9.5V star at the center of the spherelike shell. Negative feedback of the O9.5V star is also evident by the presence of a cavity (i.e., empty of molecular CO gas region) between the North and Northwest subregions. Previously, Evans & Blair (1981) also suggested that the S235 molecular cloud is heated by the exciting star. All these observed features suggest the impact of ionizing photons on the low-density regions in the complex, through which the ionized gas might have escaped.

4.2. Morphology and Signposts of Star Formation

The NIR extinction map of the S235 complex provides a more complete picture of the spatial distribution of embedded subregions. There are eight subregions that are well correlated with the locations of the dust clumps, CO gas, and YSOs. Five of these subregions (i.e., Central E, East 2, North, Northwest, and Central W) appear to be nearly regularly spaced along the spherelike shell surrounding the ionized emission. Deharveng et al. (2003) also reported a similar configuration in the Sh 104 region which was classified as a site of triggered star formation. Furthermore, three subregions (i.e., East 1, South, and Southwest) in the S235 complex are spatially away from the spherelike shell. The presence of H_2 and PAH emissions at

the boundaries of the spherelike shell indicates the presence of PDR surrounding the ionized emission (see Figure 4). In the present work, we investigated more YSOs using GPS in addition to IRAC data compared to Paper I. The YSO clusters are found in all the subregions except North, where only Class II YSOs are seen without any clustering. Additionally, the clusters of Class I YSOs are associated with the Central E, East 1, East 2, South, and Southwest subregions. The molecular data also revealed outflow signatures in the Central E, East 1, East 2, and Northwest subregions. We find the probable outflow driving candidate (i.e., Class I YSO) in each subregion. Altogether, the early stages of star formation activity are evident in all the eight subregions.

Concerning the molecular gas distribution toward the South and Southwest subregions (see Figure 7), we suggest that these two subregions seem to be located at the interface between the S235 molecular cloud ($-23\,\mathrm{km\,s^{-1}} < V_{\rm lsr} < -18\,\mathrm{km\,s^{-1}}$) and the S235AB molecular cloud ($-17\,\mathrm{km\,s^{-1}} < V_{\rm lsr} < -15\,\mathrm{km\,s^{-1}}$). As previously reported by Evans & Blair (1981), the extended star-forming region S235 is composed of two velocity components at -20 and $-17\,\mathrm{km\,s^{-1}}$. The velocity information suggests that the molecular gas associated with S235AB region is redshifted with respect to the S235 molecular cloud. In the integrated ^{12}CO map, some molecular gas is seen toward the South and Southwest subregions (see Figure 8(a)), however, the molecular gas is absent there in the integrated ^{13}CO map (see Figure 8(b)). Additionally, the A_V value is found to be significant there (see Figure 2(a)). Furthermore, the molecular gas is noticeably traced toward these subregions in a velocity range $-17\,\mathrm{km\,s^{-1}}$ to $-15\,\mathrm{km\,s^{-1}}$ (see Figure 7). In Figures 15(a) and (b), we present the distribution of molecular gas toward the "S235 complex" and the "S235AB region." The CO map is integrated in the $[-25, -15]\,\mathrm{km\,s^{-1}}$ velocity range (see Figure 15(a)). In Figure 15(b), the p–v plot of ^{13}CO gas reveals an almost broad bridge feature. The p–v plot shows that two peaks (a redshifted one and a blueshifted one as mentioned above) are separated by lower intensity intermediate velocity emission. The presence of such a broad bridge feature in the p–v plot might indicate the signature of a collision between two clouds (e.g., Haworth et al. 2015a, 2015b). Therefore, there is a possibility of the formation of YSO clusters associated with the South and Southwest subregions by the interaction between these two clouds. In the present work, our analysis is mainly focused on the S235 complex, therefore the results related to the S235AB region are not presented in this work. Hence, a detailed investigation of the interaction between these two clouds is beyond the scope of present work. It is important to note that the broad bridge feature is not seen in the p–v maps of the S235 complex (see Figure 9), suggesting the applicability of a cloud–cloud collision scenario is unlikely in the S235 complex. Hence, we rule out the cloud–cloud collision process within the S235 complex.

4.3. Triggered Star Formation

In Section 3.7, we showed that the total pressure driven by a massive star is in equilibrium with the pressure exerted by the self-gravitating molecular cloud. In Section 4.1, we discussed that the signature of the expanding H II region is evident. Additionally, we inferred that the densest subregions (i.e., East 1, East 2, and Central E) traced by NH_3 data are supersonic (see Section 3.6). We also pointed out that the observed higher velocity dispersions could be due to the presence of outflows in the subregions. Morgan et al. (2010) studied 44 bright-rimmed clouds (BRCs) using NH_3 data and found that the potentially triggered samples of BRCs are associated with higher velocity dispersions compared to non-triggered sources. In their samples, non-triggered sources were largely subsonic, whereas the triggered samples of BRCs were supersonic. These results indicate that the S235 complex could be a site of triggered star formation. This interpretation is further supported by the observed configuration as traced in the extinction map, dust continuum emission, molecular gas, ionized emission, and distribution of YSOs. Therefore, the ongoing star formation in the S235 complex may have been influenced by the expanding H II region.

Theoretically, there are two main scenarios discussed in the literature which explain the triggered star formation by the expansion of the H II region (Elmegreen 1998; Deharveng et al. 2005): "collect and collapse" (see Elmegreen & Lada 1977; Whitworth et al. 1994; Dale et al. 2007) and radiation-driven implosion (RDI; see Bertoldi 1989; Lefloch & Lazareff 1994). In the "collect and collapse" scenario, a massive and dense shell of cool neutral material can be accumulated around an expanding H II region, and star formation occurs when this material becomes gravitationally unstable. In the RDI model, the expanding H II region causes the instability and aids in the collapse of a pre-existing dense clump in the molecular cloud. Kirsanova et al. (2014) utilized NH_3 line data and suggested that the subregions (i.e., S235 East 2 and S235 Central) were formed via triggering by a "collect and collapse" process. Furthermore, they suggested that the S235 East 1 region was formed as a result of an interaction of the shock front from the S235 complex with a pre-existing dense clump.

In the present work, Bolocam data analysis revealed that the clump masses grow as one goes away from the location of the ionizing star. This pattern is observed only for those clumps which are located near the edges of the spherelike shell (e.g., the Central E, East 2, North, and Northwest subregions). It seems that the material has been collected on the edges of the spherelike shell by the expanding H II region (also see Figure 2(a)), suggesting the "collect and collapse" scenario is applicable in the complex. In order to check the "collect and collapse" process as the triggering mechanism, we calculated the dynamical age ($t_{\rm dyn}$) of the H II region and the fragmentation timescale ($t_{\rm frag}$) following the equations given in Dyson & Williams (1980, p. 204) and Whitworth et al. (1994), respectively. One can find more details of similar analysis in Dewangan et al. (2012). The condition for the "collect and collapse" process is $t_{\rm dyn} \geqslant t_{\rm frag}$. To find the values of ambient density (n_0=) for the $t_{\rm dyn} \geqslant t_{\rm frag}$ condition, the diagram of $t_{\rm frag}$ and $t_{\rm dyn}$ as a function of "n_0" is shown in Figure 15(c). The $t_{\rm frag}$ is estimated for different "a_s" values of 0.2, 0.3, and 0.4 km s^{-1} (see Section 3.6 for "a_s" estimation). Here, we use $N_{\rm uv} = 4.9 \times 10^{47}\,\mathrm{s^{-1}}$ (see Section 3.7) for the entire radio emission of the region (spatial extent ~6.′40 or 3.35 pc) and $\alpha_B = 2.6 \times 10^{-13}\,\mathrm{cm^3\,s^{-1}}$ at $T_e = 10{,}000$ K. If the condition "$t_{\rm dyn} \geqslant t_{\rm frag}$" is satisfied then the values of "n_0" should be greater than 5750, 7700, and 9240 cm^{-3} for different "a_s" values of 0.2, 0.3, and 0.4 km s^{-1}, respectively (see Figure 15(c)). On the other hand, if $n_0 < 5750\,\mathrm{cm^{-3}}$, then the condition "$t_{\rm dyn} \geqslant t_{\rm frag}$" is not fulfilled. Consequently, the fragmentation of the molecular materials into clumps will not occur due to the "collect and collapse" process in the complex.

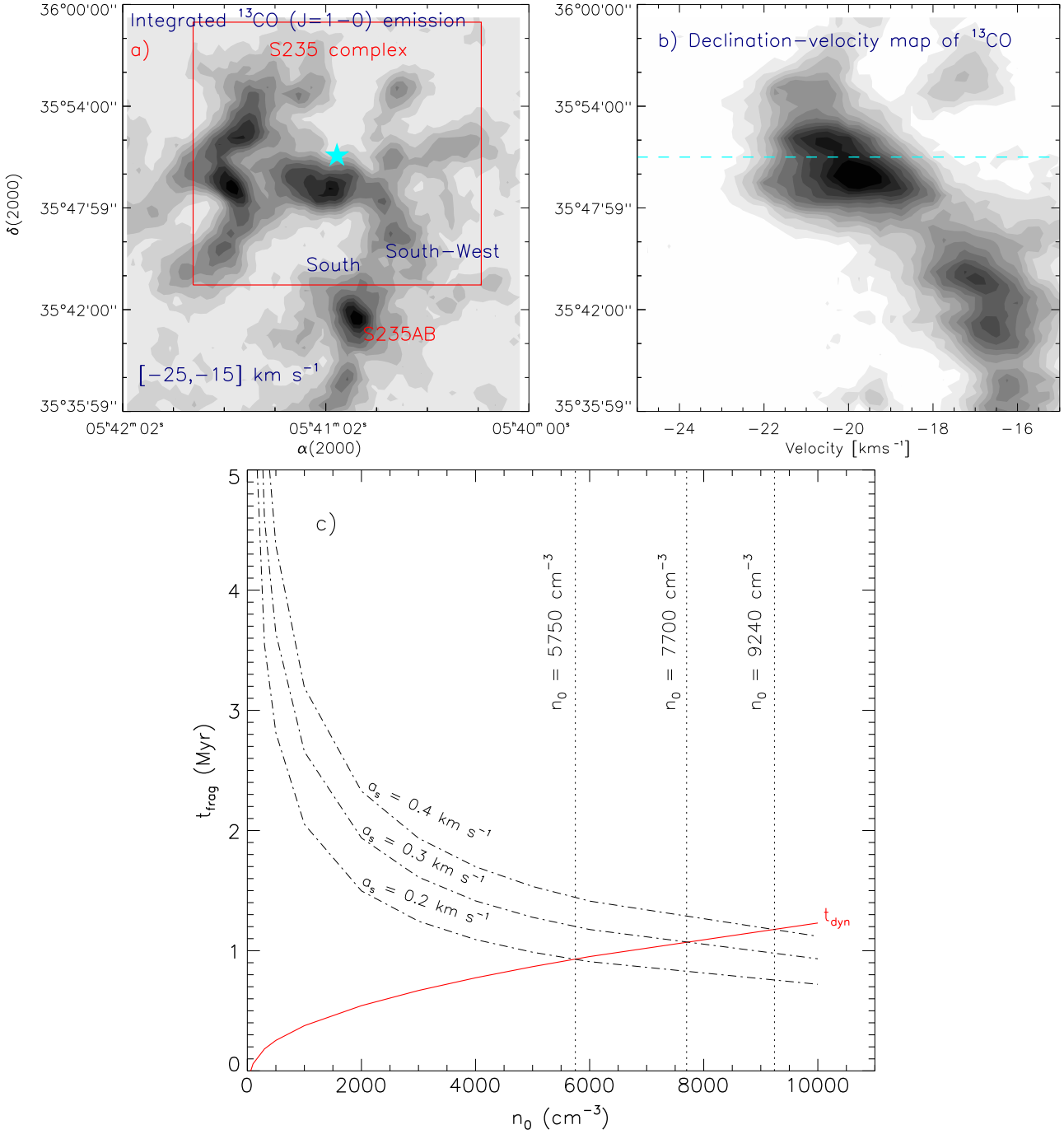

Figure 15. (a) Distribution of molecular gas toward the S235 complex and the S235AB region; a contour map of integrated ^{13}CO emission in the velocity range of −25 to −15 km s^{-1}. The location of an O9.5V star is shown by a filled star. The solid box shows the field of the S235 complex, as shown in Figure 1(a). The S235AB region is also marked in the map. (b) decl.–velocity map. The position–velocity diagram suggests the possibility of interaction between the S235 molecular cloud and the S235AB molecular cloud. (c) Plot of fragmentation timescale (t_{frag}) and dynamical time (t_{dyn}) as a function of initial density (n_0) of the ambient neutral medium. The fragmentation timescale is computed for different sound speeds of neutral gas (a_s) = 0.2, 0.3, and 0.4 km s^{-1} (see Table 2). Dotted lines depict the value of "n_0" at which "t_{dyn}" is equal to "t_{frag}" for different "a_s" values (see the text for more details).

Using ^{13}CO, NH_3, H_2CO, HCO^+, and HCN line data, a significant density variation (i.e., 1×10^3–2×10^4 cm^{-3}) has been reported in the S235 complex (Evans & Blair 1981; Kirsanova et al. 2014). Nordh et al. (1984) noted that the density structure of the S235 cloud is non-homogeneous with high density clumps engulfed in a medium with lower density. Kirsanova et al. (2014) adopted the value of volume density of 7000 cm^{-3} to compute the age of the S235 H II region. In order to compare the previous results, following Kirsanova et al. (2014), we also adopt the same value of volume density (i.e., $n_0 = 7000$ cm^{-3}) in the present work. Substituting N_{uv}, n_0, and an average radius of the H II region of $R \approx 1.67$ pc, we find $t_{dyn} \sim 1$ Myr. Our estimated t_{dyn} value is in agreement with that of Kirsanova et al. (2014). The t_{frag} is computed to be about 0.85 Myr, 1.1 Myr, and 1.3 Myr, respectively, for $a_s = 0.2$, 0.3, and 0.4 km s^{-1}. We find that the dynamical age of the H II region ($t_{dyn} \approx 1$ Myr) is comparable with the fragmentation timescale ($t_{frag} \approx$ 0.85–1.3 Myr) for $n_0 = 7000$ cm^{-3} and

a_s = 0.2–0.4 km s^{-1}. In general, the average ages of Class I and Class II YSOs are ~0.44 Myr and ~1–3 Myr (Evans et al. 2009), respectively. Considering these ages, one can notice that the dynamical age of the H II region is comparable to the ages of YSOs. These calculations suggest that the molecular materials have been fragmented into several condensations around the spherelike shell (also see Figure 13). Therefore, the "collect and collapse" scenario seems to be applicable in the S235 complex, which could be responsible for the origin of Central E, East 2, North, Northwest, and Central W subregions.

Note that the East 1 subregion is far away from the spherelike shell and is the most massive clump in the complex. Additionally, this subregion is separated from the spherelike shell by the eastern emission wall, is in pressure equilibrium, and is associated with Class I and Class II YSO clusters. This subregion is considered the youngest star-forming site in the complex (see Kirsanova et al. 2014) and is supersonic. Therefore, it seems that the YSO clusters in the East 1 subregion could originate via compression of the pre-existing dense material by the expanding H II region through the RDI process.

5. SUMMARY AND CONCLUSIONS

In this paper, we have made an extensive investigation of the S235 complex using the multi-wavelength data covering radio through NIR wavelengths. The results obtained in this work are based on the study of ionized emission, molecular emission, cold dust emission, embedded young populations, and various physical calculations. The important findings of this work are as follows.

1. The most prominent structure in the S235 complex is the spherelike shell morphology, as traced at wavelengths longer than 2 μm.
2. The distribution of ionized emission observed in the GMRT 610 MHz and NVSS 1.4 GHz continuum maps is almost spherical. The ionizing photon flux values estimated at both the frequencies correspond to a single ionizing star of O9.5V spectral type. The location of the counterpart of this ionizing star (i.e., BD +35°1201) appears at the peak of radio continuum emissions as well as approximately at the center of the spherelike shell.
3. The NIR extinction map depicts eight subregions (East 1, East 2, North, Northwest, Central W, Central E, Southwest, and South; having $A_V > 8$ mag), and five of them seem to be located in an almost regularly spaced manner along the spherelike shell surrounding the ionized emission.
4. Bolocam dust continuum emission at 1.1 mm is found toward all the eight subregions and provides more insight into the dense and cold regions of the S235 complex, which is lacking in the published sub-mm maps in the literature.
5. Bolocam clump masses increase as one moves away from the location of the ionizing star. This characteristic is found only for those clumps which are located near the edges of the shell.
6. The position–velocity analysis of ^{12}CO and ^{13}CO emissions depicts an almost semi-ringlike structure, indicating the signature of an expanding H II region.
7. The pressure calculations ($P_{\rm H\,II}$, $P_{\rm rad}$, and $P_{\rm wind}$) indicate that the photoionized gas associated with the S235 H II region can be considered the major contributor for the feedback mechanism in the S235 complex.
8. A cavity of empty molecular gas is investigated between the North and Northwest subregions, illustrating the interaction between the ionized gas and the molecular gas.
9. The mean values of Mach numbers inferred using NH_3 line data for three out of eight subregions (East 1, East 2, and Central E) are 2.9, 2.3, and 2.9, suggesting these subregions are supersonic.
10. The molecular outflows are evident in the East 1, East 2, and Central E subregions.
11. The analysis of UKIDSS-NIR and *Spitzer*-IRAC photometry reveals a total of 435 YSOs, ~59% of which are found in clusters associated with the molecular cloud.
12. In six subregions (including five located near the edges of the shell), the YSOs clusters are very well spatially correlated with the extinction, dust continuum emission, and molecular gas surrounding the ionized emission.
13. The observed configuration as traced in the extinction map, dust continuum emission, molecular gas, ionized emission, and distribution of YSOs favors the triggered star formation in the S235 complex.
14. The dynamical age of the S235 H II region ($t_{\rm dyn} \approx 1$ Myr) is comparable with the fragmentation timescale ($t_{\rm frag} \approx$ 0.85–1.3 Myr) of accumulated gas layers for ambient density (n_0) = 7000 cm^{-3} and sound speed (a_s) = 0.2–0.4 km s^{-1}.

Considering all the observational evidence presented in this work, we conclude that the S235 complex can be considered a promising nearby site of triggered star formation where both "collect and collapse" and RDI processes seem to be applicable. Additionally, the star formation activity at the interface between the S235 molecular cloud and the S235AB molecular cloud due to the cloud–cloud collision appears likely.

We thank the anonymous referee for providing useful comments, which greatly improved the scientific contents of the paper. L.K.D. acknowledges the financial support provided by the FCT (Portugal) grant SFRH/BPD/79741/2011 and the CONACYT(México) grant CB-2010-01-155142-G3. A.L. acknowledges the CONACYT(México) grant CB-2012-01-1828-41. This work is based on data obtained as part of the UKIRT Infrared Deep Sky Survey. This publication made use of data products from the Two Micron All Sky Survey (a joint project of the University of Massachusetts and the Infrared Processing and Analysis Center/California Institute of Technology, funded by NASA and NSF), archival data obtained with the *Spitzer Space Telescope* (operated by the Jet Propulsion Laboratory, California Institute of Technology under a contract with NASA). The Canadian Galactic Plane Survey (CGPS) is a Canadian project with international partners. The Dominion Radio Astrophysical Observatory is operated as a national facility by the National Research Council of Canada. The Five College Radio Astronomy Observatory CO Survey of the Outer Galaxy was supported by NSF grant AST 94-20159. The CGPS is supported by a grant from the Natural Sciences and Engineering Research Council of Canada. We thank F. Navarete for providing the narrow-band H_2 image

through the survey of extended H_2 emission from massive YSOs. We thank M.S.N. Kumar for initial discussion on the near-infrared data.

REFERENCES

Aguirre, J. E., Ginsburg, A. G., Dunham, M. K., et al. 2011, ApJS, 192, 4
Allen, L. E., Calvet, N., D'Alessio, P., et al. 2004, ApJS, 154, 363
Arce, H. G., Borkin, M. A., Goodman, A. A., Pineda, J. E., & Beaumont, C. N. 2011, ApJ, 742, 105
Bally, J., Aguirre, J., Battersby, C., et al. 2010, ApJ, 721, 137
Balser, D. S., Rood, R. T., Bania, T. M., & Anderson, L. D. 2011, ApJ, 738, 27
Beerer, I. M., Koenig, X. P., Hora, J. L., et al. 2010, ApJ, 720, 679
Bertoldi, F. 1989, ApJ, 346, 735
Bessell, M. S., & Brett, J. M. 1988, PASP, 100, 1134
Brand, J., & Blitz, L. 1993, A&A, 275, 67
Bressert, E., Bastian, N., Gutermuth, R., et al. 2010, MNRAS, 409, 54
Bressert, E., Ginsburg, A., Bally, J., et al. 2012, ApJ, 758, 28
Brunt, C. 2004, in Proc. ASP Conf. 317, Milky Way Surveys: The Structure and Evolution of our Galaxy, ed. D. Clemens, R. Shah, & T. Brainerd (San Francisco, CA: ASP), 79
Burns, R. A., Imai, H., Handa, T., et al. 2015, MNRAS, 453, 3163
Camargo, D., Bonatto, C., & Bica, E. 2011, MNRAS, 416, 1522
Carpenter, J. M. 2001, AJ, 121, 2851
Casali, M., Adamson, A., Alves de Oliveira, C., et al. 2007, A&A, 467, 777
Chavarría, L., Allen, L., Brunt, C., et al. 2014, MNRAS, 439, 3719
Chavarría, L. A., Allen, L. E., Hora, J. L., Brunt, C. M., & Fazio, G. G. 2008, ApJ, 682, 445
Condon, J. J., Cotton, W. D., Greisen, E. W., et al. 1998, AJ, 115, 1693
Dale, J. E., Clark, P. C., & Bonnell, I. A. 2007, MNRAS, 377, 535
Deharveng, L., Lefloch, B., Zavagno, A., et al. 2003, A&A, 408, 25L
Deharveng, L., Schuller, F., Anderson, L. D., et al. 2010, A&A, 523, 6
Deharveng, L., Zavagno, A., & Caplan, J. 2005, A&A, 433, 565
Dewangan, L. K., & Anandarao, B. G. 2011, MNRAS, 414, 1526
Dewangan, L. K., Luna, A., Ojha, D. K., et al. 2015, ApJ, 811, 79
Dewangan, L. K., Ojha, D. K., Anandarao, B. G., Ghosh, S. K., & Chakraborti, S. 2012, ApJ, 756, 151
Dunham, M. K., Rosolowsky, E., Evans, N. J., II, Cyganowski, C., & Urquhart, J. S. 2011, ApJ, 741, 110
Dyson, J. E., & Williams, D. A. 1980, Physics of the Interstellar Medium (New York: Halsted Press)
Elmegreen, B. G. 1998, in ASP Conf. Ser. 148, Origins, ed. C. E. Woodward, J. M. Shull, & H. A. Thronson, Jr. (San Francisco, CA: ASP), 150
Elmegreen, B. G., & Lada, C. J. 1977, ApJ, 214, 725
Enoch, M. L., Evans, N. J., II, Sargent, A. I., et al. 2008, ApJ, 684, 1240
Evans, N. J., II, Beichman, C., Gatley, I., et al. 1981, ApJ, 246, 409
Evans, N. J., II, & Blair, G. N. 1981, ApJ, 246, 394
Evans, N. J., II, Dunham, M. M., Jørgensen, J. K., et al. 2009, ApJS, 181, 321
Fazio, G. G., Hora, J. L., Allen, L. E., et al. 2004, ApJS, 154, 10
Flaherty, K. M., Pipher, J. L., Megeath, S. T., et al. 2007, ApJ, 663, 1069
Foster, T., & Brunt, C. M. 2015, AJ, 150, 147
Francesco, J. D., Johnstone, D., Kirk, H., MacKenzie, T., & Ledwosinska, E. 2008, ApJS, 175, 277
Georgelin, Y. M., Georgelin, Y. P., & Roux, S. 1973, A&A, 25, 337
Ginsburg, A., Glenn, J., Rosolowsky, E., et al. 2013, ApJS, 208, 14
Guarcello, M. G., Drake, J. J., Wright, N. J., et al. 2013, ApJ, 773, 135
Gutermuth, R. A., Megeath, S. T., Myers, P. C., et al. 2009, ApJS, 184, 18
Harper-Clark, E., & Murray, N. 2009, ApJ, 693, 1696
Haworth, T. J., Shima, K., Tasker, E. J., et al. 2015a, MNRAS, 454, 1634
Haworth, T. J., Tasker, E. J., Fukui, Y., et al. 2015b, MNRAS, 450, 10
Heyer, M., Brunt, C., Snell, R., et al. 1998, ApJS, 115, 241
Heyer, M. H., Carpenter, J. M., & Ladd, E. F. 1996, ApJ, 463, 630
Hildebrand, R. H. 1983, QJRAS, 24, 267
Indebetouw, R., Mathis, J. S., Babler, B. L., et al. 2005, ApJ, 619, 931
Israel, F. P., & Felli, M. 1978, A&A, 63, 325
Kauffmann, J., Bertoldi, F., Bourke, T. L., Evans, N. J., II, & Lee, C. W. 2008, A&A, 487, 993
Kirsanova, M. S., Sobolev, A. M., Thomasson, M., et al. 2008, MNRAS, 388, 729
Kirsanova, M. S., Wiebe, D. S., Sobolev, A. M., et al. 2014, MNRAS, 437, 1593
Klein, R., Posselt, B., Schreyer, K., Forbrich, J., & Henning, T. 2005, ApJS, 161, 361
Kumar Dewangan, L., & Anandarao, B. G. 2010a, MNRAS, 407, 1170
Kumar Dewangan, L., & Anandarao, B. G. 2010b, MNRAS, 402, 2583
Kwan, J. 1997, ApJ, 489, 284
Lada, C. J., Bergin, E. A., Alves, J. F., & Huard, T. L. 2003, ApJ, 586, 286
Lada, C. J., Lada, E. A., Clemens, D. P., & Bally, J. 1994, ApJ, 429, 694
Lada, C. J., Muench, A. A., Luhman, K. L., et al. 2006, AJ, 131, 1574
Lawrence, A., Warren, S. J., Almaini, O., et al. 2007, MNRAS, 379, 1599
Lefloch, B., & Lazareff, B. 1994, A&A, 289, 559
Lucas, P. W., Hoare, M. G., Longmore, A., et al. 2008, MNRAS, 391, 1281
Mallick, K. K., Kumar, M. S. N., Ojha, D. K., et al. 2013, ApJ, 779, 113
Marcolino, W. L. F., Bouret, J.-C., Martins, F., et al. 2009, A&A, 498, 837
Martins, F., Schaerer, D., & Hillier, D. J. 2005, A&A, 436, 1049
Matsakis, D. N., Evans, N. J., II, Sato, T., & Zuckerman, B. 1976, AJ, 81, 172
Meyer, M. R., Calvet, N., & Hillenbrand, L. A. 1997, AJ, 114, 288
Morgan, L. K., Figura, C. C., Urquhart, J. S., & Thompson, M. A. 2010, MNRAS, 408, 157
Navarete, F., Damineli, A., Barbosa, C. L., & Blum, R. D. 2015, MNRAS, 450, 4364
Nordh, H. L., van Duinen, R. J., Fridlund, C. V. M., et al. 1984, A&A, 131, 221
Paladini, R., Umana, G., Veneziani, M., et al. 2012, ApJ, 760, 149
Povich, M. S., Stone, J. M., Churchwell, E., et al. 2007, ApJ, 660, 346
Rieke, G. H., Young, E. T., Engelbracht, C. W., et al. 2004, ApJS, 154, 25
Skrutskie, M. F., Cutri, R. M., Stiening, R., et al. 2006, AJ, 131, 1163
Sugitani, K., Tamura, M., Nakajima, Y., et al. 2002, ApJL, 565, L25
Takami, M., Karr, J. L., Koh, H., Chen, H. H., & Lee, H. T. 2010, ApJ, 720, 155
Watson, C., Povich, M. S., Churchwell, E. B., et al. 2008, ApJ, 681, 1341
Whitworth, A. P., Bhattal, A. S., Chapman, S. J., Disney, M. J., & Turner, J. A. 1994, MNRAS, 268, 291
Wilson, B. A., Dame, T. M., Masheder, M. R. W., & Thaddeus, P. 2005, A&A, 430, 523
Wright, E. L., Eisenhardt, P. R. M., Mainzer, A. K., et al. 2010, AJ, 140, 1868
Zinnecker, H., & Yorke, H. W. 2007, ARA&A, 45, 481